

Demonstrating efficient and robust bosonic state reconstruction via optimized excitation counting

Tanjung Krisnanda,^{1,*} Clara Yun Fontaine,^{1,*} Adrian Copetudo,^{1,*} Pengtao Song,^{1,*}
Kai Xiang Lee,¹ Ni-Ni Huang,¹ Fernando Valadares,¹ Timothy C. H. Liew,² and Yvonne Y. Gao^{1,3,†}

¹*Centre for Quantum Technologies, National University of Singapore, Singapore*

²*Nanyang Technological University, Singapore*

³*Department of Physics, National University of Singapore, Singapore*

(Dated: March 6, 2024)

Quantum state reconstruction is an essential element in quantum information processing. However, efficient and reliable reconstruction of non-trivial quantum states in the presence of hardware imperfections can be challenging. This task is particularly demanding for high-dimensional states encoded in continuous-variable (CV) systems, as many error-prone measurements are needed to cover the relevant degrees of freedom of the system in phase space. In this work, we introduce an efficient and robust technique for optimized reconstruction based on excitation number sampling (ORENS). We use a standard bosonic circuit quantum electrodynamics (cQED) setup to experimentally demonstrate the robustness of ORENS and show that it outperforms the existing cQED reconstruction techniques such as Wigner tomography and Husimi Q-function. Our investigation highlights that ORENS is naturally free of parasitic system dynamics and resilient to decoherence effects in the hardware. Finally, ORENS relies only on the ability to accurately measure the excitation number of the state, making it a versatile and accessible tool for a wide range of CV platforms and readily scalable to multimode systems. Thus, our work provides a crucial and valuable primitive for practical quantum information processing using bosonic modes.

Continuous-variable (CV) quantum systems offer the rich and versatile dynamics of a large Hilbert space [1–4], with applications ranging across quantum computation [5, 6], metrology [7], and simulation [8]. To take full advantage of these systems, it is essential to develop techniques to accurately characterize the properties, interactions, and evolutions of their quantum states. However, reconstructing the density matrix of an arbitrary CV state in a large Hilbert space is a challenging task. Not only are many measurement observables needed to capture features spread across the large phase space, but experimentally, the observables must often be mapped to an auxiliary element (e.g. a qubit) via non-ideal and error-prone operations to extract the relevant measurement outcomes. The optimal reconstruction technique should thus consist of the fewest measurements of observables resilient against experimental error. While many different approaches to tackle this challenge have been theoretically proposed or experimentally demonstrated [9–13], these strategies often come at the cost of versatility, measurement quality, engineering convenience, and rigor of optimization.

In this work, we present a technique to robustly and efficiently reconstruct arbitrary bosonic states with the fewest, optimized measurements of excitation number. The technique can be readily implemented across CV platforms including optical photons [14], microwave photons [15–18], and phonons of trapped ions [19–21]. Our method of Optimised Reconstruction based on Excitation

Number Sampling (ORENS) is experimentally demonstrated in a cQED platform to showcase its performance for high-dimensional CV states, even under severe decoherence. We show that ORENS outperforms the state-of-the-art Wigner reconstruction technique [22, 23], owing to its inherent robustness against both coherent and incoherent errors. Our contribution to bosonic state reconstruction, a key research pillar in CV applications, will reinforce the development and analysis of more complex bosonic states, dynamics, and systems across experimental platforms.

Conceptually, reconstructing an arbitrary quantum state ρ consists of measuring identically prepared copies along many different bases. To accurately obtain information about the state, these bases must be informationally complete and the measurements have to be resilient against errors. For CV systems, when the state does not extend beyond a certain dimension D , its Hilbert space can be truncated. As such, only $D^2 - 1 := N_{obs}^*$ independent measurement observables are needed for informational completeness, setting the optimal (*) number of measurements for efficient reconstruction. To achieve independence between measurements for CV systems, the measurement observable must be changed. A convenient strategy is to apply distinct displacement transformations

$$\hat{D}(\alpha) = e^{(\alpha\hat{a}^\dagger + \alpha^*\hat{a})} \quad (1)$$

on ρ to scramble the information and sample different regions of phase space. Upon choosing a base observable and a set of displacements, the set of measurements is written as a matrix M , and the measurement process is described with Born's rule as $\vec{x} = M\vec{\rho}$, where \vec{x} is the measurement outcomes and $\vec{\rho}$ is the vectorized density

* These authors contributed equally to this article. The order of author names can be re-arranged in individual CVs.

† Corresponding author: yvonne.gao@nus.edu.sg

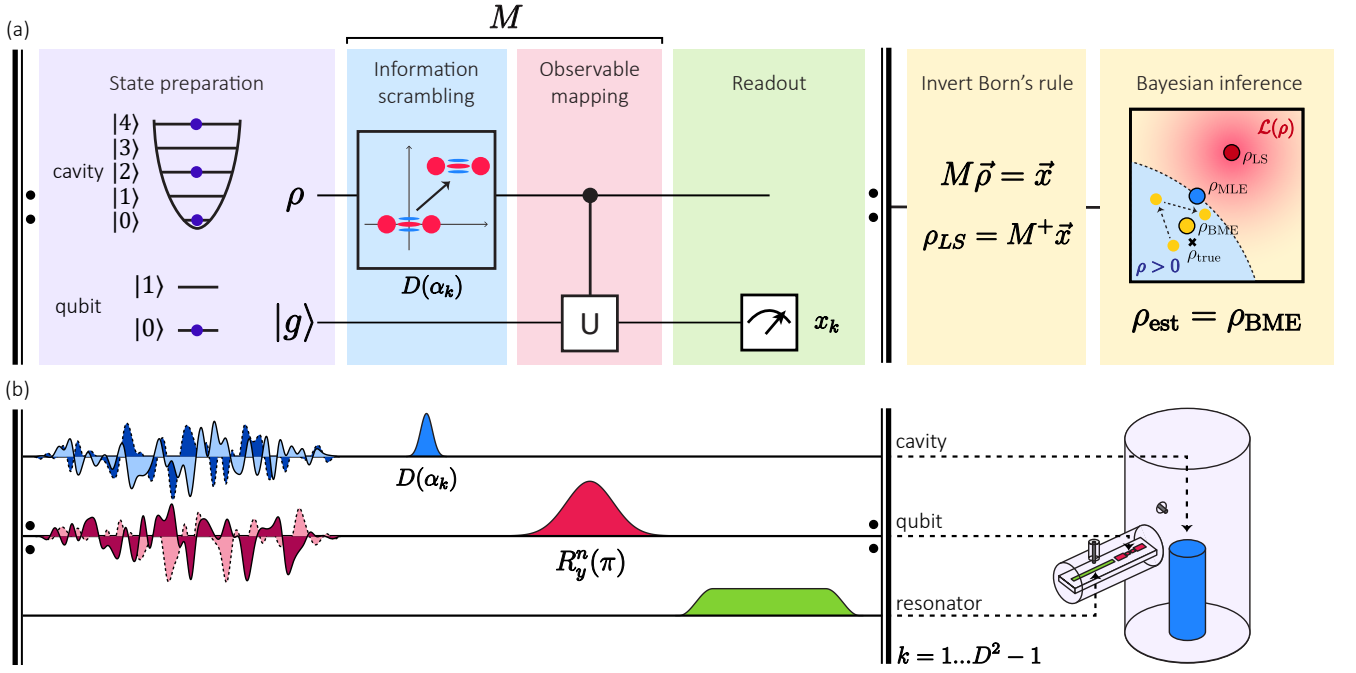


FIG. 1. **An overview of bosonic state reconstruction and its translation to ORENS in cQED.** (a) To reconstruct an arbitrary CV state ρ of dimension D , at least $D^2 - 1 := N_{obs}^*$ independent measurements must be made to be informationally complete. In bosonic systems, this is typically achieved through displacements, $D(\alpha_k)$, to N_{obs}^* distinct points in phase space which effectively changes the measurement observable. A Bayesian inference algorithm is applied to compute the optimal estimator ρ_{BME} based on the resulting measurement outcomes [24]. (b) A prototypical bosonic cQED device consists of a storage cavity (blue), an ancillary qubit (red), and a readout resonator (green). State preparation is implemented with numerically optimized pulses played to the cavity and qubit. Displacements are resonant Gaussian pulses played to the cavity. The excitation number sampling for ORENS is enacted by a conditional π -pulse on the qubit. The measurement outcome is extracted with the standard dispersive readout of the resonator.

matrix. Born's rule can be inverted to find the least-squares estimator $\vec{\rho}_{LS} = M^+ \vec{x}$, where M^+ is the Moore-Penrose pseudo-inverse of M (Appendix D1), which is constrained to be physical to realize the final estimator ρ_{est} (Appendix D3). An overview of the key bosonic state reconstruction stages is illustrated in Fig. 1a.

Ideally, N_{obs}^* independent measurements enable perfect reconstruction of ρ . However, with experimental imperfections, the accuracy of the estimated critically depends on the choice of M , which amplifies measurement errors to varying degrees upon estimation. This robustness is characterized by the condition number (CN) of the measurement matrix M , where a CN of 1 corresponds to the absence of error amplification and grants the optimal reconstruction [25].

Our proposed method, ORENS, leverages the sampling of excitation number across phase space, which is not only a readily accessible measurement observable in many CV platforms but also has built-in robustness against both decoherence and non-ideal coherent dynamics. With the minimal N_{obs}^* excitation number measurements preceded by the optimized displacements in phase space that minimize the CN to state-of-the-art (Appendix D2), ORENS is capable of reliably reconstructing the density matrix of a complex CV state.

ORENS is conceptually based on the technique of generalized Q-function [26–29], where $Q_n(\alpha) = \text{Tr}(|n\rangle\langle n| \hat{D}(\alpha)^\dagger \rho \hat{D}(\alpha))$. This is the generalization of the Husimi-Q function, $Q_0(\alpha) = \langle \alpha | \rho | \alpha \rangle$ to an arbitrary number of excitations n . Sampling higher n overcomes the limitations of Husimi Q by boosting sensitivity to phase-space oscillations of ρ . This can be understood graphically by considering that the Q_n function of a given state ρ is the convolution of the Wigner function of ρ with that of $|n\rangle$ [30]. For the specific case of vacuum $n = 0$, the Wigner of vacuum is a Gaussian distribution centered in the origin of the phase space and thus acts as a Gaussian filter on ρ , erasing fast phase-space oscillations and results in a strictly non-negative version of the Wigner function. However, for larger $n > 0$, the features of ρ are better preserved by Q_n , enabling robust reconstruction.

We validate the resilience and efficiency of ORENS by reconstructing arbitrary CV states in cQED, where excitation number is synonymous with photon number. We demonstrate that the excitation number measurement is inherently free of parasitic system dynamics and robust against decoherence. In our hardware, illustrated in Fig. 1b, the CV states are stored in the electromagnetic field of superconducting LC resonators, realized as a high-Q 3D coaxial cavity machined out of high-

purity (4N) aluminum. The states are prepared, transformed, and measured via the engineered dispersive interaction with an auxiliary qubit. The qubit is a standard transmon dispersively coupled to an on-chip readout resonator, and both elements are fabricated out of aluminum on a sapphire substrate. The full Hamiltonian of this qubit-cavity system can be found in Appendix A 4.

Extracting the excitation number of the cavity consists of conditionally exciting the qubit depending on the number of excitations in the cavity. This conditional π -pulse leverages the dispersive interaction between the cavity and qubit which can be understood by looking at the system Hamiltonian in the rotating frame of the qubit drive

$$\frac{\mathbf{H}}{\hbar} = \frac{\Omega_d}{2}\hat{\sigma}_y + \Delta|e\rangle\langle e| - \chi\hat{n}|e\rangle\langle e|, \quad (2)$$

where \hat{n} is the excitation number operator of the cavity, χ is the dispersive coupling between the cavity and the qubit, and Ω_d is the drive amplitude. By using a long, spectrally-selective drive with duration $t_\pi > 1/\chi$, the individual shifts of the qubit frequency ($\omega_q - n\chi$) corresponding to n are resolved and can be individually addressed. Choosing a drive detuning $\Delta = \chi n$ enables robust mapping of the cavity's excitation number to the qubit:

$$p_n = \text{Tr}(\rho|n\rangle\langle n|) \approx p_e(\Delta = \chi n) \quad (3)$$

where p_n is the probability of the cavity having n excitations, and p_e is the probability of the qubit being in the excited state. More details can be found in Appendix B 1.

This mapping of the excitation number does not experience significant parasitic Hamiltonian dynamics, making it an excellent choice of measurement observable for state reconstruction. To verify this, we prepare a given Fock state $|n\rangle$ in the cavity using numerically optimized GRADIENT ASCENT PULSE ENGINEERING (GRAPE) pulses [31]. We flip the qubit with a $t_\pi = 1\mu\text{s}$ Gaussian pulse selective at a frequency $\omega_q - \chi n$ to map the excitation number corresponding to $|n\rangle$ to the state of the qubit, which is read out with a single-shot measurement. We repeat the experiment 1000 times and use the average outcomes to estimate $Q_n(0)$. The results, shown in Fig. 2a, demonstrate near-perfect mapping of the excitation number from the cavity to the qubit state, with minor errors attributed to decoherence, qubit thermal population, and finite readout discrimination.

In contrast to excitation number measurement, the cavity parity measurement commonly used for the ubiquitous Wigner reconstruction is highly prone to coherent errors in the system. For the parity measurement, a $\pi/2$ pulse maps the state of the qubit (originally in $|g\rangle$) to the equator of the Bloch sphere $|+\rangle$. Then, a conditional-phase $\hat{C} = |g\rangle\langle g| \otimes \mathbb{1} + |e\rangle\langle e| \otimes e^{i\pi\hat{c}^\dagger\hat{c}}$, implemented by waiting for a time $t_w = \pi/\chi$, for the state of the qubit to acquire a relative phase, ending up in $|+\rangle(|-\rangle)$, conditioned on the cavity parity being even (odd). A final $\pi/2$ pulse maps $|+\rangle(|-\rangle)$ to $|e\rangle(|g\rangle)$. Despite this protocol being a

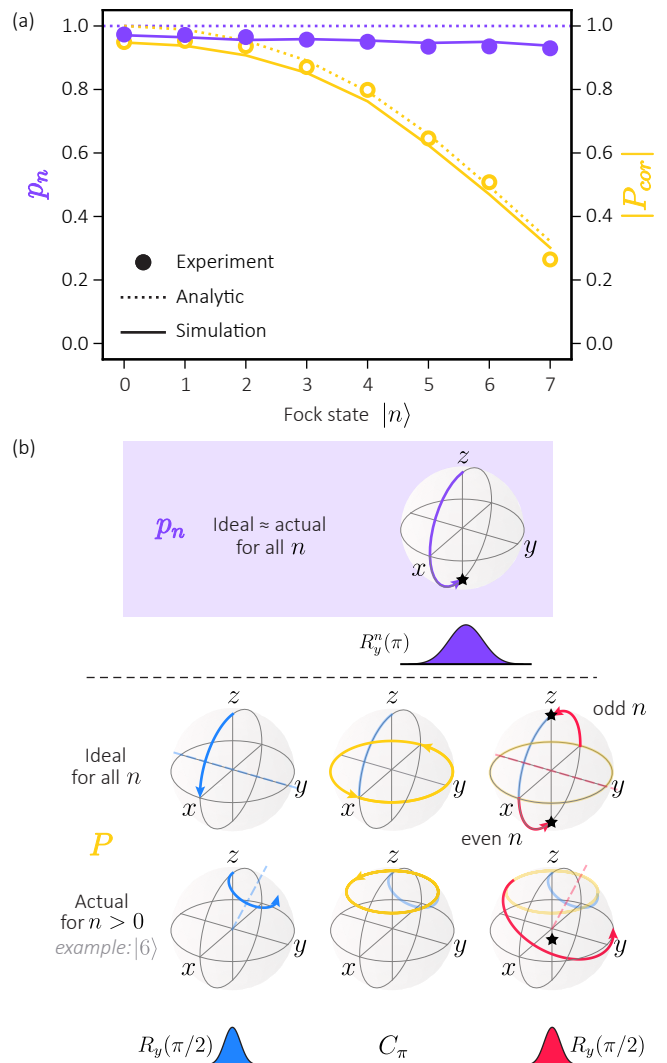


FIG. 2. Excitation number and parity mapping of Fock states in cQED. (a) Measurement outcomes of excitation number p_n (purple) and absolute value of corrected parity $|P_{cor}|$ (yellow) as a function of the Fock state $|n\rangle$ prepared in the cavity. They show good agreement with analytical (Eqn. (3) and Eqn. (4) and simulated trends based on real device parameters. (b) Bloch spheres of the qubit state at each step of excitation number (above) and parity (below) mapping. The measurement outcomes are marked with black stars.

good approximation to estimate the parity, the always-on dispersive interaction during the $\pi/2$ -pulses imparts substantial error to the measurements. To be precise, when the cavity has n excitations, the qubit rotations happen along a slanted axis $\hat{r} = (\Omega\hat{y} + \chi n\hat{z})/\sqrt{\Omega^2 + (\chi n)^2}$. As a result, the qubit state prematurely accumulates phase during the first $\pi/2$ -pulse and does not reach the equator, yielding a distorted parity approximation that degrades dramatically with increasing n , as illustrated in Fig. 2b.

A standard technique to mitigate parity measurement errors from the skewed qubit rotation is to use a wait

time $t_w < \pi/\chi$ calibrated to improve the contrast. In addition, the parity protocol can be performed twice, where the phase of the second $\pi/2$ -pulse is flipped to map even (odd) parity to $|g\rangle(|e\rangle)$, and the outcomes of the two mappings are subtracted to compute a corrected parity. However, this correction demands twice the number of measurements and still results in a scaling error of the parity,

$$P_{\text{cor}} = (P - P_{\text{inv}})/2 = \eta P_{\text{id}}, \quad (4)$$

where $P_{\text{id}} = \text{Tr}(\rho e^{i\pi\hat{n}})$, P_{inv} is the inverted parity and η is the scaling factor (Appendix B 2).

Experimentally, this degradation of parity mapping with increasing excitation number in the CV state can be readily observed. We measure the parity of a series of Fock states with the Ramsey protocol, using 16 ns $\pi/2$ -pulses and 284 ns waiting time. The results, shown in Fig. 2a, show a dramatic departure of the experimentally estimated parity from the theoretical definition of parity as the excitation number of the cavity increases. This distorted mapping makes parity a nonideal observable for state reconstruction, highlighting the importance of exploring the excitation number as a more reliable observable.

As well as being robust against coherent errors, ORENS is also robust against decoherence during the process of mapping the excitation number onto the qubit state. Here, we analyze and showcase the performance of ORENS under decoherence. In general, qubit decoherence is described by the two independent mechanisms of energy decay and dephasing, which are characterized by the coherence times T_1 and T_ϕ , respectively. While standard cQED setups can reliably achieve a T_1 in the range of several tens to hundreds of microseconds [32], ensuring a consistent T_ϕ proves to be a challenging task [33]. This challenge is particularly pronounced in the case of flux-tunable qubits, where T_ϕ can be as short as a few microseconds [34]. Considering a dephasing rate of the qubit $\Gamma_\phi = \frac{1}{T_\phi}$, using Lindblad master equation, the excitation number decays as

$$p'_n \equiv p'_e(\Delta_n = 0) \approx p_n \times \frac{1}{2}(1 + e^{-\frac{t_{\text{seq}}}{2T_\phi}}). \quad (5)$$

(Appendix C 1). This indicates that only half of the magnitude of the ideal observable (ρ_{nn}) decays exponentially with the dephasing rate.

We perform an experiment to measure p_0 of the vacuum cavity state at various engineered qubit dephasing times T_ϕ to observe the impact on the observable mapping (Fig. 3). The T_ϕ of the qubit is shortened on-demand by using excitation-induced dephasing [35], where a weak coherent tone continuously drives the readout resonator (Appendix A 6). To protect the state preparation and readout of the protocol and effectively isolate the error due to dephasing, this dephasing pulse is only applied during the mapping of the observable. The duration t_π of the π -pulse and the dispersive coupling χ are both fixed.

Our results show that excitation number mapping is partially preserved under qubit dephasing. At $T_\phi = 4\mu\text{s} = 4t_\pi$, we observe a $P_0 > 0.8$, and for as low as $T_\phi = 0.1\mu\text{s} = t_\pi/10$, the expectation value remains above 0.4. To benchmark this result, we repeat the same protocol with parity mapping. From the Lindblad master equation, we find that the whole parity observable exponentially decays to 0 (i.e. total loss of information) as T_ϕ goes to 0. Analytically, this is described by

$$P = 2p_e - 1 \approx P_{\text{id}} \times e^{-\frac{t_{\text{wait}}}{T_\phi}} \quad (6)$$

(Appendix C 1). Since parity mapping relies on the qubit state acquiring a deterministic phase, low dephasing times $T_\phi < 0.5\mu\text{s}$ completely erase this mapping, as shown in Fig. 3a.

We have thus demonstrated that excitation number mapping offers a more robust performance than the standard parity observable, indicating it is the favorable observable to measure in current state reconstruction techniques. With this, we can now use the ORENS technique to verify its ability to efficiently and accurately extract density matrices.

For a given truncated Hilbert space of dimension D , we prepare all Fock states $|k\rangle$ and their superpositions $j\rangle + e^{i\phi}|k\rangle/\sqrt{2}$ with $j < k = 0, \dots, D-1$ and $\phi = \{0, \pi/2\}$ (D^2 different states in total). Each state was experimentally prepared by playing $2\mu\text{s}$ GRAPE pulses after a qubit pre-selection pulse. Next, we perform the optimized displacements in phase space to enact the information scrambling. To obtain this set of displacements for a given truncation dimension D , we sweep over the excitation number $n \in [1, D-1]$, where for each set n we run a gradient-descent algorithm over the set of displacements $\{\alpha_k\}_{k=1}^{N_{\text{obs}}^*}$ to minimize the CN of M . This set of measurements allows us to reconstruct any arbitrary state bounded by dimension D . As an example, the optimal displacements for $D = 6$ are 35 unique $\{\alpha_k\}_{k=1}^{35}$ each followed by a measurement of excitation number $n = 5$. The different displacements $\{\alpha_k\}$ were implemented using a 240 ns Gaussian coherent pulse at the cavity frequency by varying its amplitude and phase. Upon applying the displacement, the qubit was flipped conditionally on the n^{th} excitation population of the cavity, and then measured through single-shot low-power dispersive readout. The measurement outcomes were processed to estimate ρ , first by inverting Born's rule to obtain the least-squares estimator ρ_{LS} , and then by using Bayesian inference [24] to obtain ρ_{BME} as our final reconstructed estimator. The Bayesian method treats uncertainty in meaningful ways and utilizes all available information optimally, ultimately returning the most optimal estimator for ρ [36, 37], particularly in comparison to the ubiquitous maximum likelihood estimation approach [38] (Appendix D 3).

To evaluate the quality of the state reconstruction, we compute the fidelity between the estimated density matrix and the target density matrix ρ_{tar} , generated by

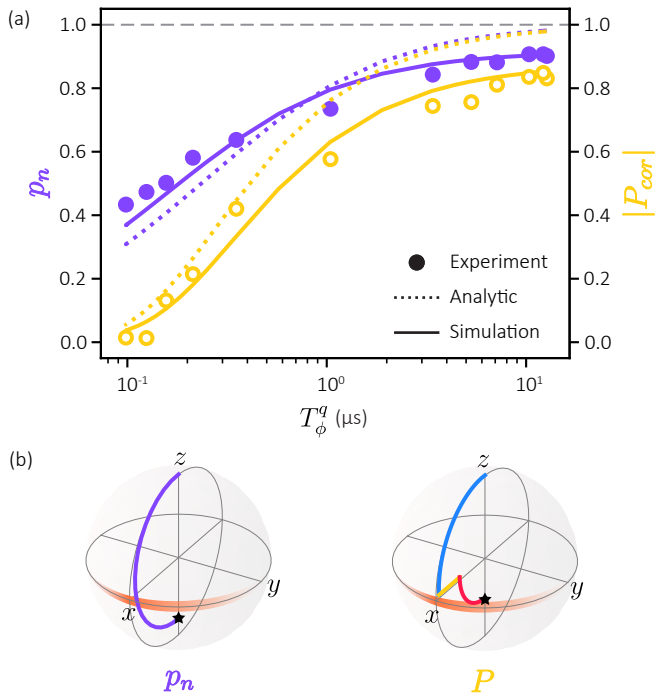


FIG. 3. **Excitation number and parity under qubit dephasing.** (a) The measurement outcomes of excitation number p_n (purple) and absolute value of corrected parity $|P_{cor}|$ (yellow) mappings are plotted against varying T_ϕ of the qubit. They show good agreement with analytical (Eqn. (5) and Eqn. (6) and simulated trends based on real device parameters. With roughly half the contrast preserved, excitation number measurements are partially robust against qubit dephasing in cQED, whereas parity mapping suffers significantly more degradation. (b) Intuitive illustrations for the resilience shown by excitation number mapping. The qubit state spends less time near the equator (orange) in mapping p_n than P , and thus is less susceptible to dephasing.

simulating the GRAPE pulses under decoherence with QuTiP,

$$F = \left(\text{Tr} \sqrt{\sqrt{\rho_{\text{tar}}} \rho_{\text{BME}} \sqrt{\rho_{\text{tar}}}} \right)^2. \quad (7)$$

The average fidelity over the D^2 different states for each dimension is plotted in Fig. 4a, up to $D = 6$. Beyond $D = 6$, the readout was distorted due to the dominant cross-interaction between the cavity and the readout resonator present for larger bosonic states, resulting in the absence of meaningful experimental points. This is not a fundamental limitation of the technique but a rather device-specific artifact. The dominant error mechanisms impacting the reconstruction fidelity are the thermal population of the qubit and imperfect single-shot readout discrimination (Appendix A 7, C 2), which could be significantly reduced by improving device thermalization and using a quantum-limited amplifier, respectively. Across all dimensions, the reconstruction fidelity using ORENS exceeds 95%.

Having tested the reconstruction technique on superpositions of Fock states, we evaluate the protocol for cat states, a versatile backbone of CV information processing protocols [39–43]. We repeat the same reconstruction protocol for $D = 6$ with four small cat states: $|\alpha\rangle \pm |\alpha\rangle$ and $|\alpha\rangle \pm i|\alpha\rangle$, with $\alpha = 1$ and normalization. The averaged fidelity matches the Fock state superposition fidelities, see the purple star in Fig. 4.

We benchmark the reconstruction performance of both Fock and cat states against two versions of the standard Wigner protocol, normal and corrected. For normal Wigner, we fix the measurement observable to parity and optimize the corresponding N_{obs}^* displacements for information scrambling. For corrected Wigner, the distortion of the always-on dispersive interaction is partially corrected for by using and subtracting both the parity and inverse parity protocols with the same set of N_{obs}^* displacements, to have an overall set of $2N_{obs}^*$ independent measurements (i.e. double the theoretical minimum). The measurement matrices for Wigner and ORENS had roughly equal condition numbers, indicating that neither parity nor excitation number are theoretically limited. Thus, the reconstruction fidelity must be limited by experimental errors.

With a focus on reconstruction with the minimal number of measurements N_{obs}^* , ORENS demonstrates accurate reconstruction across dimensions, significantly surpassing the performance of the normal Wigner protocol. Only the corrected Wigner tomography, which demands double the number of independent measurements, demonstrates comparable state reconstruction to ORENS.

To further investigate state reconstruction under qubit dephasing, we prepare the same four cat states and reconstruct them using ORENS for the different qubit T_ϕ points previously calibrated, see Fig. 4b. Remarkably, we notice only a slight deterioration of the average reconstruction fidelity, with fidelities resting $> 86\%$. This demonstrates that even when using a conditional π -pulse duration that far exceeds the dephasing time of the qubit, the excitation number observable still maps enough information to robustly reconstruct states under severe dephasing.

The robustness under dephasing implies the versatility of the ORENS in regimes of low- χ between the cavity and the qubit. To maintain an equivalent frequency-selectivity, a smaller value of χ demands a longer t_π . Considering our experimental (simulated) fidelity of 88% (92%) with $\chi = 1.4$ MHz and $T_\pi/T_\phi = 1\mu\text{s}/0.5\mu\text{s} = 2$, we can expect an equivalent fidelity with $\chi = 35$ kHz, $T_\pi/T_\phi = 40\mu\text{s}/20\mu\text{s} = 2$. This was verified with a simulation to reconstruct the cat states, with an average fidelity of 94%.

Through the above analytic and experimental results, we have demonstrated: (1) technique for Optimized Reconstruction with Excitation Number Sampling (ORENS) with minimal measurements that relies only on displacements and excitation counting, and can be read-

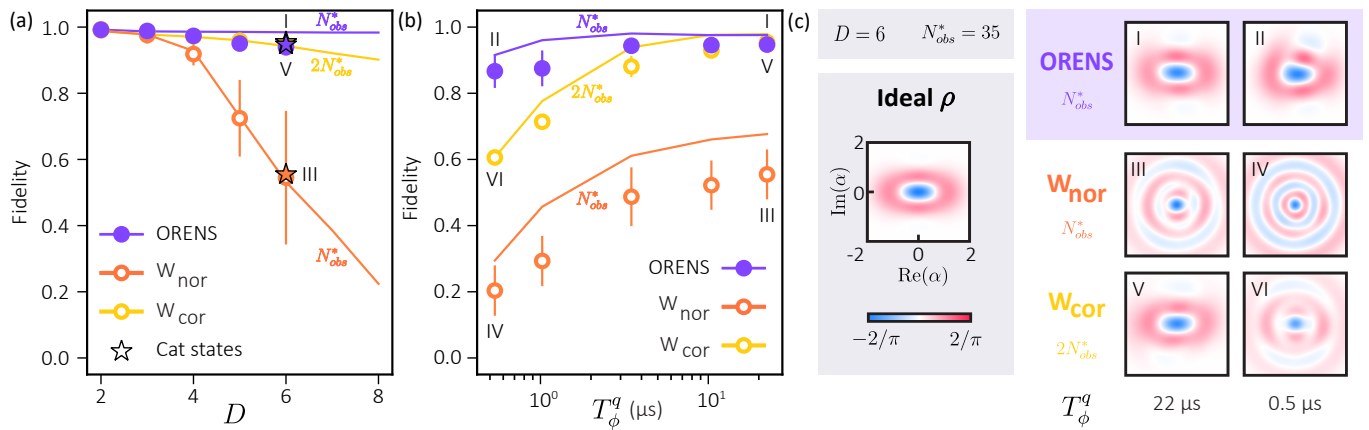


FIG. 4. **State reconstruction for ORENS (N_{obs}^*), normal Wigner (N_{obs}^*), and corrected Wigner ($2N_{\text{obs}}^*$).**

(a) The average reconstruction fidelities for D^2 different states (Fock states and their superpositions) against cut-off dimension D . They show good agreement with simulated trends based on real device parameters. The star markers are average fidelities for reconstructing four small cat states, well contained within $D = 6$. Beyond $D = 6$, there are no meaningful experimental points as the readout was distorted by cross-Kerr between the readout resonator and cavity. (b) The average reconstruction fidelities of the four small cat states for different qubit dephasing times T_ϕ . (c) Wigner functions of the reconstructed odd cat states ($|\alpha\rangle - |-\alpha\rangle$) with ORENS, normal Wigner, and corrected Wigner techniques at two different T_ϕ points. With strong retention of important cat state properties, ORENS outperforms both Wigner reconstruction techniques with the fewest measurements, particularly at high dimensions and under qubit dephasing.

ily applied across CV experimental platforms, (2) excitation number mapping in bosonic cQED is an ideal and convenient observable for state reconstruction that can be directly implemented on standard devices without any tailored operations or parameters, (3) excitation number can partially be mapped even under severe qubit dephasing in cQED, and (4) ORENS reliably reconstructs arbitrary states of all dimensions even under severe qubit dephasing in cQED.

For each of the experiments, ORENS outperforms the state-of-the-art parity and Wigner reconstruction with the fewest measurements. While the fidelity of the state obtained with ORENS is nearly matched with the corrected Wigner strategy, our method uses half the number of measurements and scales more favorably with state dimensionality. The primary drawback of ORENS in cQED is the high sensitivity to undesired residual excitations of the qubit (Appendix C2). However, the reconstruction fidelity can be readily improved with good thermalization of the qubit as well as standard pre-selection measurements.

Looking beyond, the ORENS can be readily implemented for multimode systems. For example, for a two-mode system A and B , each with dimension D , we would apply the displacements $\{D_A(\alpha_i) \otimes D_B(\alpha_j)\}$, where $\{\alpha_i\}$ is the optimized single-mode amplitudes, before measuring the optimized joint excitation numbers. In cQED, the joint excitation numbers are directly extracted with a selective π pulse tuned to $\omega_q - n_A\chi_A - n_B\chi_B$. Not only would this multimode reconstruction approach likely outperform the standard joint Wigner tomography for similar arguments of excitation number observable robustness, but the measurement of joint excitation number is

significantly more convenient than joint parity. Joint parity measurements are challenging, as they require either designing $\chi_A = \chi_B$ or utilizing higher levels of the transmon with concatenated single-mode conditional phase gates [13]. While the generalized Wigner function [11] helps overcome these practical challenges, the arbitrary relative phase of the modified Ramsey sequence tend to reduce the contrast of measurement outcomes and renders the reconstruction less robust.

Furthermore, ORENS is naturally compatible with other techniques to simplify the complexity of bosonic state tomography. It is often more interesting to retrieve only partial knowledge of a system, rather than performing full state reconstruction. For instance, to characterize particular features in phase space like the fringes of a cat state [44]. ORENS is easily modified for these cases by changing the phase-space region of displacement optimization, as well as the prior knowledge and likelihood function in Bayesian inference. A similar modification can be made for incorporating feedback such that the next measurements are informed by the previous ones.

Overall, we have developed and demonstrated a versatile technique to efficiently and robustly estimate arbitrary CV states, accessible across different bosonic hardware platforms. Our results bring us one step closer to scalable and reliable characterization and verification across CV quantum applications.

ACKNOWLEDGMENTS

Y.Y.G. acknowledges the funding support of the National Research Foundation grant number NRF2020-NRF-ISF004-3540 and the Ministry of Education, Singapore grant number MOE-T2EP50121-0020. T.K. thanks Tomasz Paterek for discussions during the earlier stages of this project.

APPENDIX A: Experimental Device

1. Design and tools

The experimental device used in this work is a standard bosonic cQED system[45, 46] in the strong dispersive-coupling regime. It consists of a superconducting microwave cavity, dispersively coupled to a transmon qubit for controllability and readout, which is also dispersively coupled to a planar readout resonator. We simulate the electromagnetic fields of the device using Ansys finite-element High-Frequency Simulation Software (HFSS) and obtain the Hamiltonian parameters using the energy participation ratio (EPR) approach [47]. The key system properties, such as the frequency of each circuit and the pair-wise non-linear couplings between them, are iteratively refined to meet the target parameters. In this section, we describe the details of the design considerations, the resulting properties of the main elements in the device, and the main calibration procedures for the different experimental parameters.

2. Package and chip fabrication

The storage cavity is a three-dimensional high-Q coaxial $\lambda/4$ -resonator with a cut-off frequency $f_{\text{cut}} \sim 600$ MHz. The cavity and the coaxial waveguide that hosts the qubit and the resonator are machined out of high-purity (5N) aluminum, where the external layer (0.15 mm) has been removed with chemical etching to reduce fabrication imperfections. The ancillary transmon qubit and the planar readout resonator are fabricated by evaporating aluminum on a sapphire substrate. The design is patterned using a Raith electron-beam lithography machine, on a HEMEX sapphire substrate cleaned with 2:1 piranha solution for 20 minutes and coated with 800 nm of MMA and 250 nm of PMMA resist. The pattern is then developed with a mixture of de-ionized water and isopropanol at a 3:1 ratio. Using a PLASSYS double-angle evaporator we deposit the two aluminum layers of 20 nm and 30 nm thickness at -25 and +25 degrees, respectively, separated by an oxidation step with a mixture of 85% O_2 and 15% Argon at 10 mBar for 10 minutes. The chip is finally diced on an Accretech machine and inserted in the waveguide, with an aluminum clamp where we use indium wire to improve thermalization.

3. Intrinsic Purcell filtering

The design of the Hamiltonian parameters considers the ORENS protocol requirements and the versatility to explore different decoherence regimes. We design the dispersive interaction between the cavity and the qubit to be ~ 1.4 MHz. Hence, our selective pi-pulses need to be $\sim 1\mu\text{s}$ -long, and the Ramsey revival time $\sim \frac{\pi}{\chi} \approx 3.14\mu\text{s}$.

To achieve long-enough coherence times for the qubit, we mitigate its resonator-mediated Purcell decay by designing an intrinsic Purcell-filter structure [48]. This is done by optimizing the position of the coupled transmission line. Simulations show that the optimal position aligns with the voltage node of the qubit field at approximately $\lambda_{\text{qubit}}/4$ away from the end of the resonator. In this position, the qubit field is very weakly coupled to the transmission line while the readout resonator is significantly coupled for fast readout.

For ease of fabrication and to preserve cavity coherence, the transmission line is kept at an appropriate distance. To satisfy this requirement, as well as the strong dispersive coupling and the intrinsic-purcell filtering condition at the same time, we added two planar stripline-like structures on both ends of the qubit pads. The strips are short enough not to introduce any mode below 8 GHz, while effectively guiding the transmon field to the cavity and to readout resonator modes as desired.

4. Hamiltonian parameters and coherence times

Expanding the cosine term of the Josephson junction up to the fourth order, we can write the full Hamiltonian of our system as

$$\begin{aligned} \frac{\hat{H}}{\hbar} = & \omega_c \hat{c}^\dagger \hat{c} + \omega_q \hat{q}^\dagger \hat{q} + \omega_r \hat{r}^\dagger \hat{r} \\ & - \frac{\chi_{cc}}{2} \hat{c}^\dagger \hat{c}^\dagger \hat{c} \hat{c} - \frac{\chi_{qq}}{2} \hat{q}^\dagger \hat{q}^\dagger \hat{q} \hat{q} - \frac{\chi_{rr}}{2} \hat{r}^\dagger \hat{r}^\dagger \hat{r} \hat{r} \\ & - \chi_{cq} \hat{c}^\dagger \hat{c} \hat{q}^\dagger \hat{q} - \chi_{qr} \hat{q}^\dagger \hat{q} \hat{r}^\dagger \hat{r} - \chi_{cr} \hat{c}^\dagger \hat{c} \hat{r}^\dagger \hat{r}, \end{aligned} \quad (\text{A1})$$

where the $\omega_c, \omega_q, \omega_r$ respectively denotes the angular frequencies of the cavity, qubit, and resonator, and the χ_{ij} of the second and third lines correspond to the self-Kerr and cross-Kerr interactions between modes, respectively. The value of the experimentally calibrated parameters can be seen in tables I and II.

	$\omega/2\pi(\text{GHz})$	$T_1(\mu\text{s})$	$T_2(\mu\text{s})$	$T_2^{\text{echo}}(\mu\text{s})$
Qubit	5.277	85-113	14-22	44-48
Cavity	4.587	992	-	-
Readout	7.617	2.08	-	-

TABLE I. Frequency and coherence times for the 3 modes of the device.

The next major contribution to Eqn. (A1), stemming from the sixth-order term of the cosine expansion, corresponds to the second-order dispersive interaction between

	Cavity	Qubit	Resonator
Cavity	4-6 kHz	1.423 MHz	2 kHz
Qubit	1.423 MHz	175.3 MHz	0.64 MHz
Readout	2 kHz	0.64 MHz	-

TABLE II. Table of Kerr interactions. Diagonal elements correspond to the self-Kerr interactions of each mode, and off-diagonal terms correspond to the cross-Kerr interactions between different modes.

the cavity and the qubit, $-\chi'_{cq} q^\dagger q c^\dagger c^\dagger c c$. By fitting the resonance frequencies of the qubit to second order on the number of excitations in the cavity, we find $\frac{\chi'_{cq}}{2\pi} \approx 16$ kHz.

5. Microwave wiring

The radio-frequency (RF) pulses to drive the readout resonator, qubit, and cavity are created by IQ-mixing the local oscillator (LO) signal from a Vaunix Lab Brick microwave resonator with the intermediate-frequency (IF) I and Q quadratures generated by the Digital-to-Analogue Converter (DAC) port of a Quantum Machines fast field-programmable gate array (FPGA). For the readout, we measure the reflected signal from the resonator, which is amplified in a High-electron mobility transistor (HEMT) amplifier and a room-temperature ZVA-183S+ amplifier before being down-converted to 50 MHz with a Marki IR-mixer. The signal is finally amplified with a Stanford Research Systems SR445A room-temperature amplifier before being sampled in the Analogue-to-Digital Converter (ADC) block of the FPGA. The schematic wiring setup can be seen in Fig. 5.

6. Engineering qubit dephasing

To demonstrate the robustness of ORENS under qubit dephasing, we engineer the dephasing time T_ϕ of the qubit. This is achieved by driving the dispersively-coupled readout resonator to a steady-state photon population that induces dephasing via photon-shot noise. The dephasing rate is controlled by varying the average excitation number in the resonator [35].

To calibrate the average excitation number \bar{n} in the resonator as a function of the drive amplitude, we populate the resonator with a square pulse and conduct a Ramsey experiment. Subsequently, we fit the modulated Ramsey oscillations using the free parameter \bar{n} [49]. For a given drive amplitude A_d – expressed as the voltage of the DAC output –, we can extract \bar{n} as a function of the pulse length, see Fig. 6a. For all drive amplitudes, the resonator reaches a steady state after $2.5 \mu\text{s}$, which is set as the ring-up time $\tau_{rp} = 2.5 \mu\text{s}$. Following a similar calibration, we choose the ring-down time τ_{rd} for resonator decay as $2.5 \mu\text{s}$.

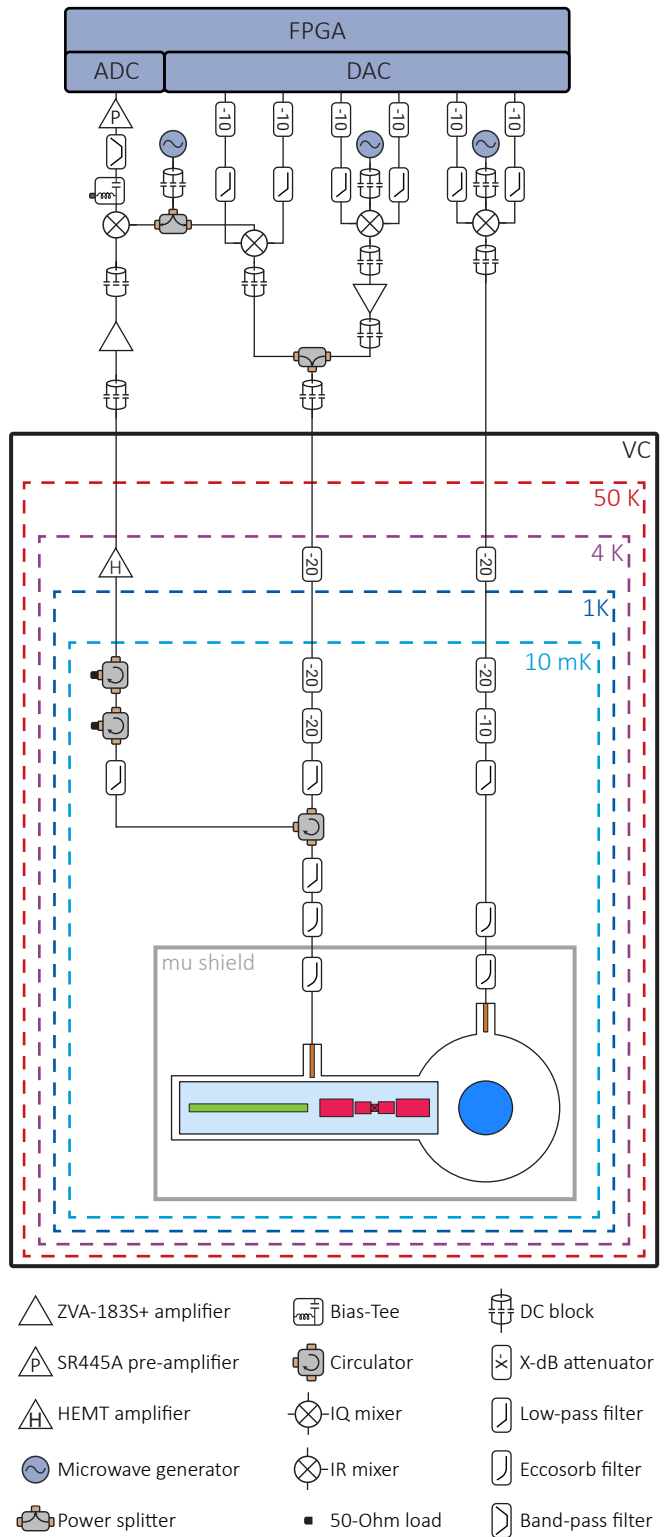


FIG. 5. **Experimental setup.** Schematic of the RF components and connections at room temperature and inside the Bluefors dilution refrigerator.

Driving the resonator not only induces qubit dephasing but also shifts the qubit frequency due to its dis-

persive interaction. As shown in the qubit spectroscopy plot in Fig. 6b measured with the sequence in d, the qubit peak broadens and shifts with increasing drive amplitude A_d . To isolate the dephasing effect from the frequency-shifting effect in the experiments that follow, we perform the observable mapping protocols using the shifted frequency corresponding to the resonator drive amplitude.

To characterize the qubit's pure dephasing time $T_\phi = 1/(1/T_2 - 0.5/T_1)$ for each resonator drive, we measure the qubit energy relaxation time T_1 and qubit dephasing time T_2 after driving the resonator to steady state and updating the qubit frequency (pulse sequences in Fig. 6d). As shown in Fig. 6c, T_1 stays relatively constant with increasing resonator drive amplitude, while T_2 decreases smoothly. This indicates the photon-shot noise in the resonator only induces qubit dephasing, not qubit energy relaxation.

Having calibrated how to engineer T_ϕ , we now study how the measurement observables – excitation number p_n for ORENS and parity P for Wigner – behave when increasing the qubit dephasing rate while keeping the cavity in vacuum state, see Fig. 3 in the main text. The pulse sequence is shown in Fig. 7a. For a certain calibrated T_ϕ , we drive the resonator to steady state, update the qubit frequency, and conduct the standard p_n and P observable mapping protocols. Then, after a ring-down time t_{rd} for the resonator to de-populate, the measurement pulse is applied.

We evaluate ORENS and Wigner state reconstruction under dephasing, see Fig. 4 in the main text, using the pulse sequence in Fig. 7b. To mitigate the error due to the qubit thermal population, we first measure the qubit state to later post-select the data. After waiting a delay time t_d for the resonator to decay, we prepare the small cat states using GRAPE pulses with a length of $2 \mu\text{s}$. After state preparation, we drive the resonator to steady state to induce a reduced T_ϕ , apply a displacement pulse to the cavity, and perform either the p_n or P mapping. Then, we turn off the resonator drive and wait a ring-down time t_{rd} for the resonator decay, before applying a final measurement pulse.

7. Error budgeting

We use a standard square low-power readout pulse at the resonance frequency of the readout resonator when the qubit is in the ground state. The length of the readout pulse is $1.5 \mu\text{s}$ and the reflected signal is acquired for a total time of $2.4 \mu\text{s}$. We measure a readout fidelity is $F_{\text{RO}} = 1 - (P(e|g) + P(g|e))/2 = 96.5 \%$, of which we estimate an infidelity of 1.9% due to thermal population, 1.4% due to readout discrimination error (overlap), and 0.4% due to qubit decay during the readout.

The cavity was measured to have a 3% residual population, i.e. $p_1=3\%$. The cavity states were prepared with numerical pulses optimized with the GRAPE algorithm applied simultaneously at the qubit and the cavity,

with a fixed total duration of $2 \mu\text{s}$, for all states. The average residual thermal population of the qubit after the GRAPE pulses is measured to be 4.9%, and is further attenuated down to 3% by performing a $1.5 \mu\text{s}$ -long readout before the numerical pulses and pre-selecting only those runs where the qubit was measured in the ground state. We calibrated a $2.5 \mu\text{s}$ -long buffer time between the readout pulse and the GRAPE pulses for the resonator to de-populate. We test the quality of the state preparation by simulating the effect of the numerical pulses with the whole qubit-cavity Hamiltonian accounting for decoherence and thermal populations. The fidelity in relation to the ideal pulses can be seen in Fig. 8. The 3% infidelity for preparing the cavity in vacuum (Fock 0 in the figure) can be explained by the previously-mentioned thermal population of the cavity, and it matches the discrepancy between the experimental data and the ideal value in Fig. 2 in the main text. In addition, the experimental p_n data shows a slow systematic decay as a function of Fock state, which can be explained by state preparation errors of the GRAPE pulses, see Fig. 8.

APPENDIX B: Coherent error in observables

1. Excitation number mapping and its selectivity

Here we show the expression for the qubit probability following the excitation number mapping protocol, show how it maps to excitation number of the cavity state, and discuss its selectivity. We set $\hbar = 1$ henceforth.

First, we start with a dynamics that will be useful later on. In particular, on a qubit alone, with a Hamiltonian $\hat{H} = \Delta|e\rangle\langle e| + (\Omega/2)\hat{\sigma}_y$ and initial state $|g\rangle$ one can calculate its dynamics and confirm that the probability in the excited state at time t is

$$p_e(t) = \frac{\Omega^2}{\Omega^2 + \Delta^2} \sin^2(\sqrt{\Omega^2 + \Delta^2} \frac{t}{2}). \quad (\text{B1})$$

At $t_{\text{sel}} \equiv \pi/\Omega$, the probability is maximum ($p_e = 1$) for $\Delta = 0$ and decays as the detuning $|\Delta|$ increases.

Now, the Hamiltonian for sampling the excitation number of the cavity state is

$$\hat{H} = \Delta|e\rangle\langle e| + \frac{\Omega}{2}\hat{\sigma}_y - \chi|e\rangle\langle e| \otimes \hat{a}^\dagger \hat{a}. \quad (\text{B2})$$

The sequence starts with the qubit in $|g\rangle$ and cavity in any state ρ . The qubit state at time t follows

$$\begin{aligned} \rho_q(t) &= \text{tr}_{\text{cav}}(e^{-i\hat{H}t}(|g\rangle\langle g| \otimes \rho) e^{i\hat{H}t}) \\ &= \sum_n \langle n|e^{-i\hat{H}t}(|g\rangle\langle g| \otimes \rho) e^{i\hat{H}t}|n\rangle \\ &= \sum_n p_n e^{-i\hat{H}_n t} |g\rangle\langle g| e^{i\hat{H}_n t}, \end{aligned} \quad (\text{B3})$$

where tr_{cav} is partial trace with respect to the cavity state, $p_n \equiv \langle n|\rho|n\rangle$ denotes the diagonal elements (excitation number) of ρ , and $\hat{H}_n \equiv \Delta_n|e\rangle\langle e| + (\Omega/2)\hat{\sigma}_y$ now acts only on the qubit with $\Delta_n \equiv \Delta - \chi n$.

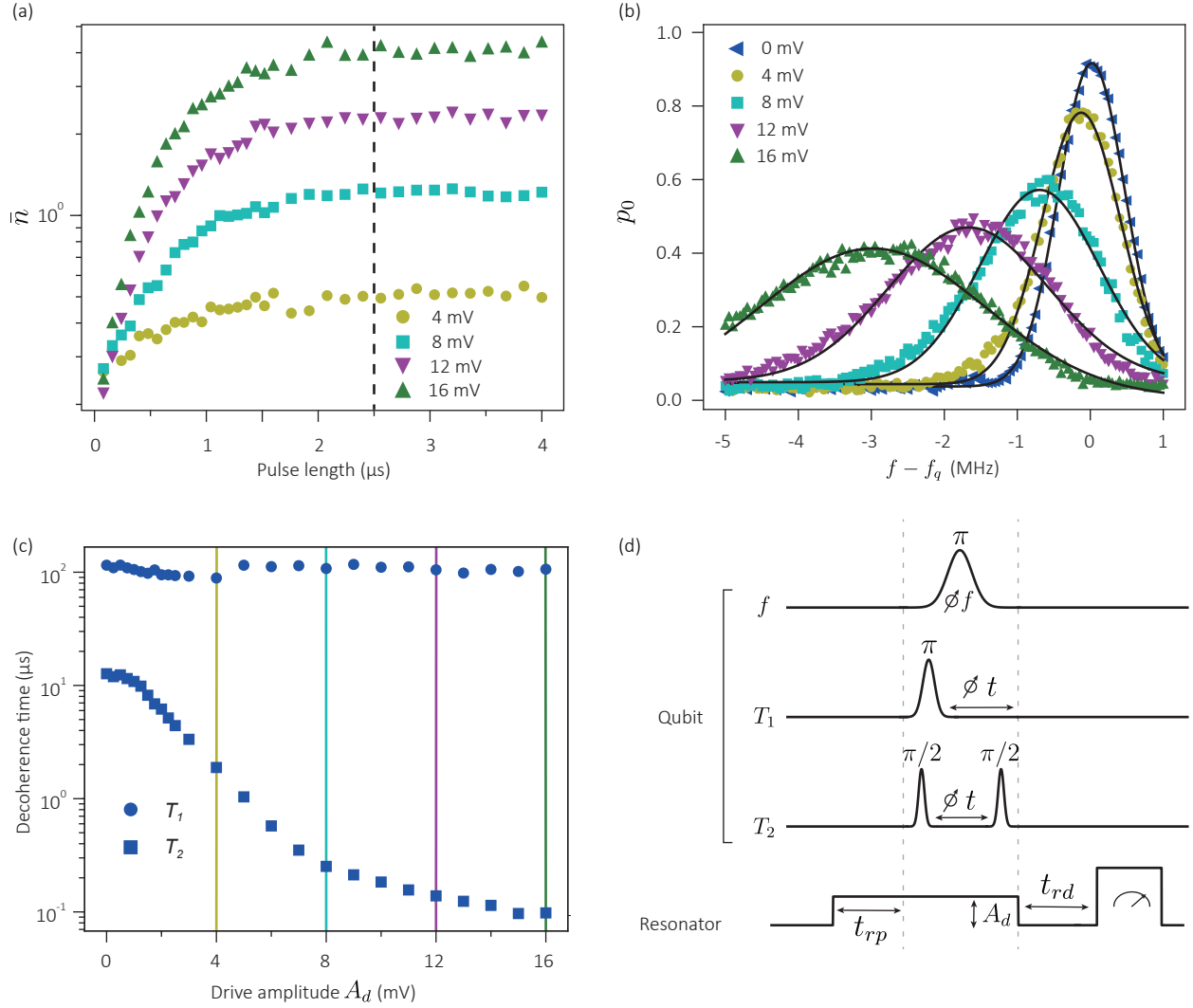


FIG. 6. **Engineering qubit dephasing.** (a) The average excitation number \bar{n} in the resonator with various pulse lengths and drive amplitude A_d of the square pulse (method from Ref. [49]). The resonator population reaches a steady state at ring-up time t_{rp} across all A_d . The black dotted line indicates the ring-up time t_{rp} we take is 2.5 μs . (b) The qubit spectra after driving the resonator to steady state with square pulses of varying drive amplitudes with Gaussian fits. The measurement pulse sequence is shown in (d), where the ring-up time t_{rp} and the ring-down time t_{rd} are both 2.5 μs , and the length of the π pulse 1 μs . (c) The qubit energy relaxation time T_1 and qubit dephasing time T_2 with varying resonator drives. The vertical lines correspond to the drive amplitudes used in (a) and (b). The qubit T_1 and T_2 are measured with the pulse sequences in (d) after driving the resonator to steady state.

The probability of the qubit in excited state at time $t_{\text{sel}} = \pi/\Omega$ then reads

$$\begin{aligned}
 p_e &= \sum_n p_n |\langle e | e^{-i\hat{H}_n t_{\text{sel}}} | g \rangle|^2, \\
 &= \sum_n p_n \frac{\Omega^2}{\Omega^2 + \Delta_n^2} \sin^2(\sqrt{\Omega^2 + \Delta_n^2} \frac{t_{\text{sel}}}{2}), \quad (\text{B4})
 \end{aligned}$$

where we have made use of Eqn. (B1). Each component in the summation of Eqn. (B4) features a function whose maximum value is p_n at $\Delta_n = \Delta - \chi n = 0$ and it decays as $|\Delta_n|$ increases. This means that the position of the maximum value (with respect to Δ) for each component is different. In the case where the decay is enough, e.g.,

when $\chi/\Omega \gg 1$, different components do not affect each other, and we say that the excitation number sampling is selective. The qubit probability can then be approximated as

$$p_e(\Delta_n = 0, t_{\text{sel}}) \approx p_n, \quad (\text{B5})$$

which is the basis for the mapping of excitation number.

The formula in Eqn. (B4) can also be written as

$$p_e = \sum_n p_n \frac{1}{1 + \eta^2} \sin^2(\sqrt{1 + \eta^2} \frac{\pi}{2}), \quad (\text{B6})$$

in terms of $\eta \equiv \Delta_n/\Omega = (\Delta - \chi n)t_{\text{sel}}/\pi$. If we rescale the detuning $\Delta' \equiv \Delta t_{\text{sel}}$ (simply a stretch in the function, i.e.,

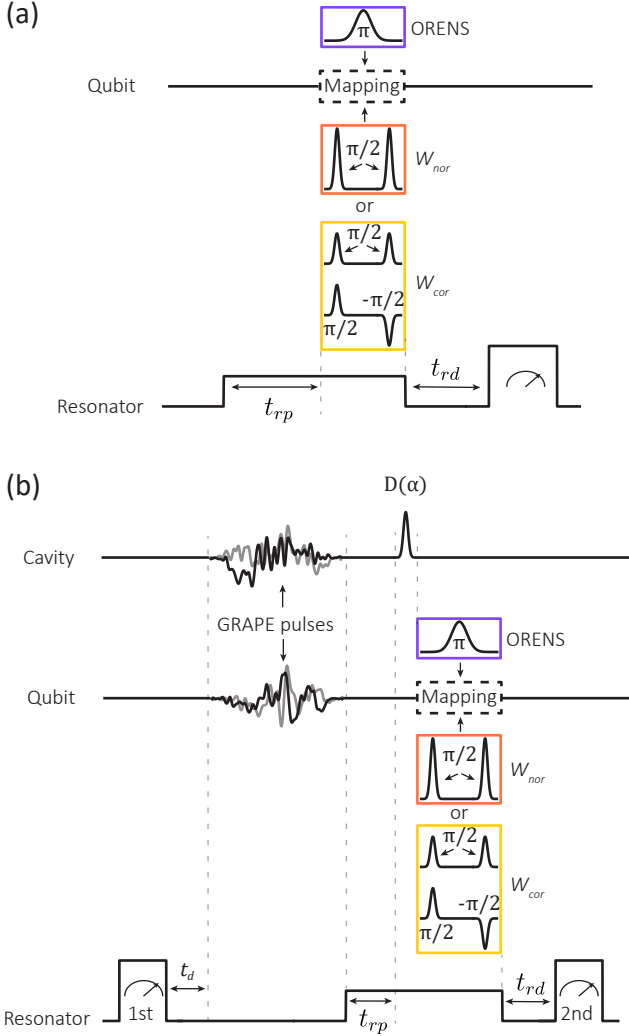


FIG. 7. **Pulse sequences with engineered qubit dephasing for observable mapping and state reconstruction.**

(a) The pulse sequence for ORENS and Wigner observable mapping (Fig. 3). The ring-up time t_{rp} and the ring-down time t_{rd} are both $2.5 \mu\text{s}$, the lengths of the π pulse and the $\pi/2$ pulse are $1 \mu\text{s}$ and 64 ns respectively, and the delay time τ for parity measurement is 284 ns . (b) The pulse sequence ORENS and Wigner state reconstruction (Fig. 4(b) and (c)). We apply an additional measurement pulse to the resonator at the start for post-processing selection. The delay time t_d for the resonator decay after the first measurement, the ring-up time t_{rp} , and the ring-down time t_{rd} are both $2.5 \mu\text{s}$. The length of the GRAPE pulses is $2 \mu\text{s}$, the length of the displacement pulse $D(\alpha)$ is 240 ns , the lengths of the π pulse and the $\pi/2$ pulse are $1 \mu\text{s}$ and 64 ns respectively, and the delay time τ for parity measurement is 284 ns .

selectivity is the same), $\eta = (\Delta' - n\chi t_{\text{sel}})/\pi$. It is clear that Eqn. (B4), up to a stretch, is determined simply by χt_{sel} . For instance, this means that having larger χ (more selective) is equivalent to having the duration of the protocol t_{sel} longer. Also, having low χ (less selective) can be compensated by having longer t_{sel} .

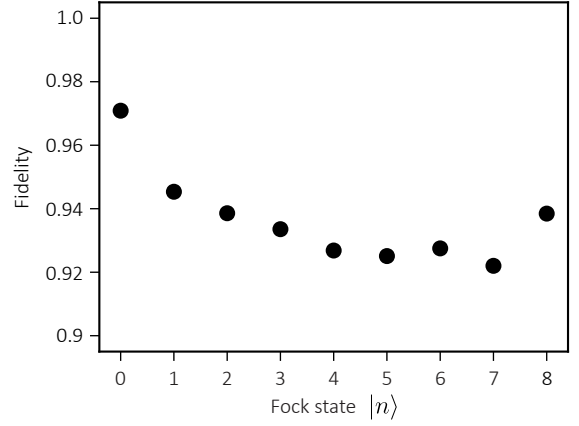


FIG. 8. **State preparation.** GRAPE state preparation fidelities for the Fock states.

2. Parity mapping

Similarly, in this section, we provide expressions for the qubit probability and show how they map to the parity of the cavity state. We will also show that the mapping is inaccurate, which is caused by coherent errors that manifest as scaling and offset to the ideal parity.

Parity mapping is done with $\pi/2$ -wait- $\pi/2$ pulse sequence. Let us first consider an ideal case in which the Hamiltonian for the $\pi/2$ pulses is $\hat{H}_p = (\Omega/2)\hat{\sigma}_y$ applied for $t_{\pi/2} = \pi/(2\Omega)$, while for the wait it is $\hat{H}_d = -\chi|e\rangle\langle e| \otimes \hat{a}^\dagger \hat{a}$ applied for a time $t_w = \pi/\chi$. The initial state for the sequence is qubit in $|g\rangle$ and cavity in any state ρ . Essentially, the $\pi/2$ pulses each realize a $\pi/2$ rotation on the qubit (along the \hat{y} axis on the Bloch sphere). During the wait, a conditional phase gate $\hat{C} = |g\rangle\langle g| \otimes \mathbb{1} + |e\rangle\langle e| \otimes \hat{P}$, where $\hat{P} = e^{i\hat{a}^\dagger \hat{a}}$, is implemented. By solving for the qubit-cavity state, one can get the expression for the probability of the qubit in the excited state:

$$p_e = \frac{1}{2}(1 + P), \quad (\text{B7})$$

where $P \equiv \text{tr}(\rho \hat{P})$ denotes the parity of the cavity state ρ . The expression in Eqn. (B7) presents an ideal mapping between the qubit probability and the parity. Its alternate form is $P = -\langle \hat{\sigma}_z \rangle$, i.e., even (odd) parity states are mapped to the south (north) pole of the Bloch sphere of the qubit.

However, with the always-on dispersive coupling the Hamiltonian during the $\pi/2$ pulses is $\hat{H}_{pd} = (\Omega/2)\hat{\sigma}_y - \chi|e\rangle\langle e| \otimes \hat{a}^\dagger \hat{a}$, which introduces a coherent error for the parity mapping. A standard technique to partially counter this is to reduce the duration during the wait $t_w < \pi/\chi$. Solving for the qubit-cavity state with the actual Hamiltonian \hat{H}_{pd} during the $\pi/2$ pulses and variable time t_w during the wait becomes less complicated and insightful when considering a special in which the cavity is in the number state $\rho = |n\rangle\langle n|$. In this case, we derive

the state of the qubit after the sequence to arrive at the

following parity mapping:

$$\begin{aligned} P' &\equiv -\langle \hat{\sigma}_z \rangle \\ &= f_1(\xi) \cos(\chi n t_w) - f_2(\xi) \sin(\chi n t_w) - f_3(\xi) \end{aligned} \quad (\text{B8})$$

where $\xi \equiv \chi n / \Omega$ and

$$\begin{aligned} f_1 &= \frac{1}{(1 + \xi^2)^2} \left(\sin^2\left(\frac{\pi}{2} \sqrt{1 + \xi^2}\right) + 2\xi^2 \cos\left(\frac{\pi}{2} \sqrt{1 + \xi^2}\right) (1 - \cos\left(\frac{\pi}{2} \sqrt{1 + \xi^2}\right)) \right), \\ f_2 &= \frac{2\xi}{(1 + \xi^2)^{3/2}} \sin\left(\frac{\pi}{2} \sqrt{1 + \xi^2}\right) (1 - \cos\left(\frac{\pi}{2} \sqrt{1 + \xi^2}\right)), \\ f_3 &= \frac{\left(\xi^2 + \cos\left(\frac{\pi}{2} \sqrt{1 + \xi^2}\right)\right)^2}{(1 + \xi^2)^2}. \end{aligned} \quad (\text{B9})$$

It is easy to see that in the limit of infinitely short $\pi/2$ pulses ($\xi \rightarrow 0$) and $t_w = \pi/\chi$, the parity reduces to the ideal value: $P' = \cos(n\pi) = (-1)^n = P$. In general, f_1 is the main term that contains most of the ideal parity, f_2 is a term that corrects the parity by choosing a shorter wait time $t_w < \pi/\chi$, and f_3 is simply an offset term that shifts the parity (both positive and negative) in one direction. To illustrate the values of f_1 , f_2 , and f_3 for higher Fock states, we plot these coefficients against ξ in Fig. 9. For a high enough Fock state, the offset term dominates and the parity reduces to $P' \rightarrow -1$. By identifying the roles of these coefficients, we can conveniently define errors for the parity as

$$P' = P \eta - \zeta, \quad (\text{B10})$$

where η is a scaling error that incorporates the main and correction terms f_1 and f_2 , whereas ζ is an offset error coming from f_3 .

By reversing the second $\pi/2$ pulse in the sequence, i.e., using $\hat{H}_{pd} = -(\Omega/2)\hat{\sigma}_y - \chi|e\rangle\langle e| \otimes \hat{a}^\dagger \hat{a}$, the parity now reads

$$\begin{aligned} P'_{\text{rev}} &\equiv -\langle \hat{\sigma}_z \rangle \\ &= -f_1(\xi) \cos(\chi n t_w) + f_2(\xi) \sin(\chi n t_w) - f_3(\xi). \end{aligned} \quad (\text{B11})$$

By using both P and P_{rev} , we can correct the offset error as

$$\begin{aligned} P'_{\text{cor}} &\equiv \frac{P' - P'_{\text{rev}}}{2} \\ &= f_1(\xi) \cos(\chi n t_w) - f_2(\xi) \sin(\chi n t_w) \\ &= P \eta. \end{aligned} \quad (\text{B12})$$

However, the scaling error remains.

We experimentally observe P' and the impact of the scaling and offset errors by measuring the parity of a series of Fock states with the Ramsey protocol, using 16 ns $\pi/2$ -pulses and 264 ns waiting time. In the results, shown

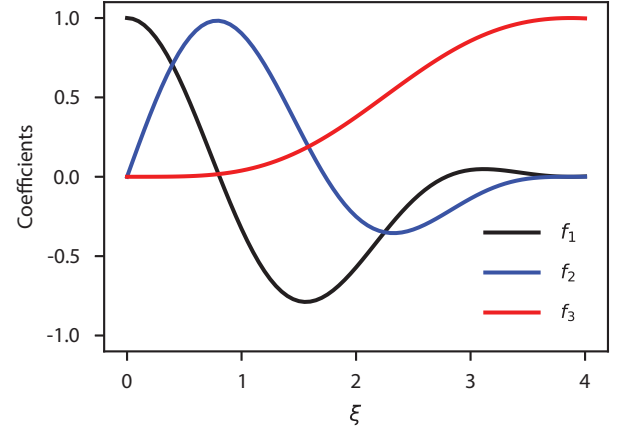


FIG. 9. Coefficients for the parity in Eqn. (B9) against $\xi = \chi n / \Omega$.

in Fig. 10a, scaling error shows up as a decrease in overall contrast, and offset error appears as the skew between the even and odd Fock states. Fig. 10b is an illustration of how the measurements of the even Fock states are degraded more significantly with higher n than the odds. This is due to the tilted rotation axis asymmetrically impacting the Ramsey evolutions of the evens and the odds. If we were to flip the mapping of the evens and odds to the qubit measurement outcomes, then the odd Fock states would degrade more significantly.

APPENDIX C: Incoherent error in observables

1. Qubit dephasing T_ϕ

The primary limitation of excitation number sampling is qubit decoherence. This stems from the frequency-selectivity imposed by the finite dispersive coupling χ .

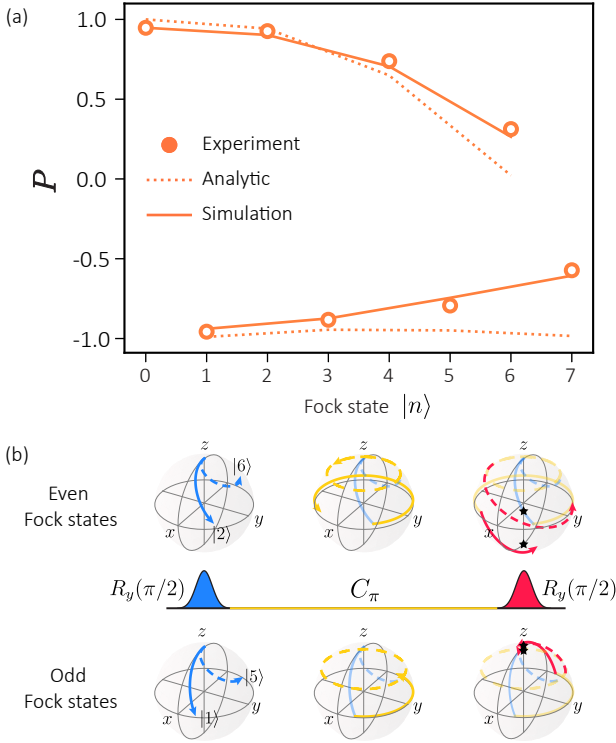


FIG. 10. **Parity coherent errors.**(a) Measurement outcomes of parity P under scaling and offset errors as a function of Fock state $|n\rangle$ prepared in the cavity. They show good agreement with analytical (Eqn. (B10)) and simulated trends based on real device parameters. (b) Bloch spheres of the qubit state at each step of the parity mapping for even and odd Fock states. The mapping of the even states suffers more due to the offset error.

To be precise, coherence time imposes a limit on the maximum π -pulse duration before the qubit decoheres. The maximum pulse duration sets the frequency bandwidth, and thus selectivity, of the pulse. Because the qubit frequency shifts by χn for each excitation n of the cavity, the maximum selectivity of the pulse then sets the minimum dispersive frequency shift χ necessary to resolve the excitation number.

For the qubit, there are two loss channels to consider: energy decay and dephasing, which are characterized by their respective coherence times T_1 and T_ϕ . While standard cQED setups can reliably achieve T_1 s in the range of several tens to hundreds of microseconds [32], ensuring a consistent T_ϕ proves to be a challenging task [33]. In what follows, we will analyze the excitation number and parity mapping only under qubit dephasing.

In the case of excitation number, we recall Eqn. (B3) in Appendix B 1, which with added qubit dephasing can be written as

$$\begin{aligned}
 \rho_q(t_{\text{sel}}) &= \sum_n \langle n | \cdots \hat{U}_{\Delta t} \varepsilon(\hat{U}_{\Delta t} \varepsilon(|g\rangle\langle g| \otimes \rho) \hat{U}_{\Delta t}^\dagger) \hat{U}_{\Delta t}^\dagger \cdots |n\rangle \\
 &= \sum_n \langle n | \rho |n\rangle \left(\cdots \hat{U}_{n,\Delta t} \varepsilon(\hat{U}_{n,\Delta t} \varepsilon(|g\rangle\langle g|) \hat{U}_{n,\Delta t}^\dagger) \hat{U}_{n,\Delta t}^\dagger \cdots \right), \\
 p'_e(t_{\text{sel}}) &= \sum_n p_n \langle e | \left(\cdots \hat{U}_{n,\Delta t} \varepsilon(\hat{U}_{n,\Delta t} \varepsilon(|g\rangle\langle g|) \hat{U}_{n,\Delta t}^\dagger) \hat{U}_{n,\Delta t}^\dagger \cdots \right) |e\rangle,
 \end{aligned} \tag{C1}$$

where the step-by-step is explained as follows. The dynamics in the first line is essentially a repetitive action of infinitesimal loss channel and unitary. One can think of the loss channel in the Kraus representation, where $\varepsilon(\cdot) \equiv \sum_j E_j \cdot E_j^\dagger$ with E_j the Kraus operator, while the short unitary is simply $\hat{U}_{\Delta t} \equiv e^{-i\hat{H}\Delta t}$ with a small time interval $\Delta t = t_{\text{sel}}/N$ and $N \rightarrow \infty$. We then note that the loss channel only acts on the qubit, while $\hat{U}_{\Delta t}$ with the number operator $\hat{a}^\dagger \hat{a}$ in the Hamiltonian can act on the Fock states $|n\rangle$. This important observation allows for the simplification leading to the second line, where $\hat{U}_{n,\Delta t} \equiv e^{-i\hat{H}_n \Delta t}$ with $\hat{H}_n = \Delta_n |e\rangle\langle e| + (\Omega/2) \hat{\sigma}_y$ only

acting on the qubit. The third line then presents the qubit probability and cavity excitation mapping, analogous to Eqn. (B4) in Appendix B 1.

Note that the third line in Eqn. (C1) can be written as $p'_e(t_{\text{sel}}) = \sum_n p_n w_n$, where the weight w_n is the probability of the qubit being in excited state, where its dynamics starts in $|g\rangle$ with a Hamiltonian \hat{H}_n under dephasing loss. Just like in Section II.1, with the selectivity assumption, we arrive at

$$p'_e(\Delta_n = 0) \approx p_n w, \tag{C2}$$

where the weight w is obtained in the same way as w_n but with a Hamiltonian $\hat{H} = (\Omega/2) \hat{\sigma}_y$ under dephasing.

This way, qubit dephasing scales the probability of all excitation number p_n with the same magnitude.

To get the weight w , we can solve the qubit dynamics under decoherence conveniently with the Lindblad mas-

$$\begin{aligned} w &= \frac{1}{2}(1 - e^{-\gamma\pi}(\cos(\sqrt{1-\gamma^2}\pi) + \frac{\gamma}{\sqrt{1-\gamma^2}}\sin(\sqrt{1-\gamma^2}\pi)), \text{ for } \gamma < 1, \\ w &= \frac{1}{2}(1 - e^{-\gamma\pi}(\frac{\gamma + \sqrt{\gamma^2-1}}{2\sqrt{\gamma^2-1}}e^{\sqrt{\gamma^2-1}\pi} + \frac{-\gamma + \sqrt{\gamma^2-1}}{2\sqrt{\gamma^2-1}}e^{-\sqrt{\gamma^2-1}\pi})), \text{ for } \gamma > 1, \end{aligned} \quad (\text{C4})$$

where $\gamma \equiv 1/(2T_\phi\Omega)$ and the first (second) line represents the small (over) dephasing case. In most cases, we have small dephasing such that (up to the second order in γ) the weight can be approximated as $w \approx (1 + e^{-\gamma\pi})/2$, and the mapping

$$p'_n \equiv p'_e(\Delta_n = 0) \approx p_n \times \frac{1}{2}(1 + e^{-\frac{t_{\text{sel}}}{2T_\phi}}). \quad (\text{C5})$$

In the case of parity mapping, for simplicity let us assume that the $\pi/2$ pulses are perfect, i.e., they are $\pi/2$ rotations of the qubit along \hat{y} axis on the Bloch sphere. This is because the pulses are ideally much shorter in duration compared to the wait. Considering qubit dephasing only on the wait simplifies the derivation considerably as this only degrades the off-diagonal elements of the qubit density matrix during the wait by e^{-t_w/T_ϕ} . Consequently, after solving for the qubit state, the parity mapping follows

$$P' \equiv 2p'_e - 1 = P \times e^{-\frac{t_w}{T_\phi}}. \quad (\text{C6})$$

2. Qubit thermal population

Both excitation number and parity mapping rely on the qubit initialized in the ground state $|g\rangle$. In reality, the qubit might be in a mixed state with some probability being in the excited state before the mapping protocol is performed. In our experiments, this type of error comes from imperfect state preparation using GRAPE. To analyze this further, we will assume that the initial state before the mapping is $\rho_{qth} \otimes \rho$, where $\rho_{qth} = (1-\lambda)|g\rangle\langle g| + \lambda|e\rangle\langle e|$ with λ being the probability of the qubit being in the excited state.

For excitation number mapping, following the deriva-

tion equation

$$\dot{\rho} = -i[H, \rho] + \hat{J}\rho\hat{J}^\dagger - \frac{1}{2}\{\rho, \hat{J}^\dagger\hat{J}\}, \quad (\text{C3})$$

where $\hat{J} \equiv \sqrt{2/T_\phi}|e\rangle\langle e|$ is the jump operator for qubit dephasing. Solving for the qubit state this way translates to solving a second-order differential equation. After a tedious but straightforward calculations, the weight is given by

tion in Eqn. (B3), now we have

$$\begin{aligned} p'_e(t) &= \\ &\sum_n p_n \langle e|e^{-i\hat{H}_n t}((1-\lambda)|g\rangle\langle g| + \lambda|e\rangle\langle e|) \otimes \rho e^{i\hat{H}_n t}|e\rangle. \end{aligned} \quad (\text{C7})$$

When evaluating the term $\langle e|\dots|e\rangle$ in the summation at $t_{\text{sel}} = \pi/\Omega$, we note two cases: (i) at $\Delta_n = 0$ and (ii) at $\Delta_n \gg \Omega$. For (i), the unitary is $e^{-i\hat{H}_n t_{\text{sel}}} = e^{-i\hat{\sigma}_y \pi/2}$, which is a π rotation of the qubit. In this case, we have $\langle e|\dots|e\rangle = 1 - \lambda$. For (ii), the unitary is $e^{-i\hat{H}_n t_{\text{sel}}} \approx e^{-i\Delta_n t_{\text{sel}}}|e\rangle\langle e|$. In this case, we have $\langle e|\dots|e\rangle = \lambda$. Both (i) and (ii) are essential for the excitation number mapping:

$$p'_n \equiv p'_e(\Delta_n = 0) = (1-\lambda)p_n + \lambda \sum_{j \neq n} p_j, \quad (\text{C8})$$

where the biggest contribution comes from p_n with weight $1 - \lambda$ accompanied by small contributions from other excitation probabilities $p_{j \neq n}$ each with weight λ as they are far away from $\Delta_n = 0$ (we assume $\Delta_n \gg \Omega$). By noting that $\sum_{j \neq n} p_j = (1 - p_n)$ ($\text{tr}(\rho) = 1$), we have

$$p'_n = p_n(1 - 2\lambda) + \lambda, \quad (\text{C9})$$

where we see that the thermal population of the qubit introduces a scaling and offset error to the ideal excitation number. However, if λ is known, the excitation number measurement can be corrected as $p_n = (p'_n - \lambda)/(1 - 2\lambda)$, where p'_n is the measured value.

For parity, solving the dynamics starting with the qubit in a mixed state can be done component-by-component. For the $(1 - \lambda)$ component, the qubit starts in $|g\rangle\langle g|$ and the parity is given by Eqn. (B7). On the other hand, for the λ component, we can follow similar steps and arrive at $p_e = (1 - P)/2$. By combining both contributions, we have

$$p'_e = (1 - \lambda)\frac{1 + P}{2} + \lambda\frac{1 - P}{2}. \quad (\text{C10})$$

This means for the parity mapping, we have

$$P' \equiv 2p'_e - 1 = (1 - 2\lambda)P, \quad (\text{C11})$$

which means that thermal population of the qubit only results in a scaling error for the parity. Similarly, if λ is known the parity can also be corrected as $P = P'/(1 - 2\lambda)$, where P' is the measured value.

APPENDIX D: Estimator for ρ

1. Linear inversion

The oldest and simplest procedure to build an estimator for ρ is called linear inversion. This method consists of interpreting the relative frequencies of measurement outcomes as probabilities and then inverting Born's rule through a least-squares (LS) inversion to obtain a ρ_{LS} that predicts these probabilities.

Born's rule relates the outcome probability p_k of a certain measurement observable \hat{E}_k to ρ :

$$p_k = \text{Tr}(\rho \hat{E}_k) \quad (\text{D1})$$

Upon many measurement repetitions, we build a histogram and approximate each p_k with the corresponding relative frequency of outcome k . For ORENS, each measurement observable is defined with a displacement $\hat{D}(\alpha_k)$ and excitation number n . We can write \hat{E}_{n,α_k} as $\hat{E}_{n,\alpha_k} = \hat{D}_{\alpha_k} |n\rangle\langle n| \hat{D}_{-\alpha_k}$ and the corresponding probability $p_n = \text{tr}(\hat{E}_{n,\alpha_k} \rho)$. Let us define a measurement matrix M to describe the set of ORENS measurements as

$$\begin{pmatrix} \vec{E}_{n,\alpha_1} \\ \vec{E}_{n,\alpha_2} \\ \vdots \\ \vec{E}_{n,\alpha_{D^2-1}} \end{pmatrix}. \quad (\text{D2})$$

with dimensions $(D^2 - 1) \times D^2$ where \vec{E} is the row-wise vectorized form of \hat{E} . Then, vectorizing ρ column-wise to get $\vec{\rho}$ of length D^2 and writing the outcome probabilities as \vec{p} of length $D^2 - 1$, we can then write the matrix equation

$$M\vec{\rho} = \vec{p} \quad (\text{D3})$$

Linear inversion corresponds to inverting this system using the observed relative frequencies \vec{p} to derive $\vec{\rho}$. Because M is not square, the system is solved using the Moore-Penrose pseudoinverse as

$$\vec{\rho} = (M^\dagger M)^{-1} M^\dagger \vec{p} = M^+ \vec{p} \quad (\text{D4})$$

For $M^\dagger M$ to be invertible, the measurement observables must be independent i.e. the set of measurements must be informationally complete. In our work, we parameterize and vectorize ρ with the real and imaginary

parts of the elements above the diagonal, as well as all but the last diagonal elements to obtain a vector \vec{Y} of the length of $D^2 - 1$. Different parameterizations of ρ are related linearly as $\vec{\rho}$ to \vec{Y} as $\vec{\rho} = K\vec{Y} + \Theta$. Plugging this into Eqn. (D3), and replacing MK with W and $M\Theta$ with V , we obtain a modified linear equation $W\vec{Y} + V = \vec{p}$ that we used in our work.

2. Optimizing set of measurements

The measurement observables for ORENS are optimized using gradient-descent over the displacements and excitation number n to minimize the condition number (CN) of W , where the condition number captures the degree of error amplification. An example code will be made available on GitHub soon.

The CN achieved by ORENS across dimensions is comparable to that of Wigner, indicating they have near-equivalent theoretical reconstruction capabilities (Fig. 11). However, the optimal CN for Husimi Q-function scales unfavorably beyond $D > 2$, illustrating that robust reconstruction is infeasible.

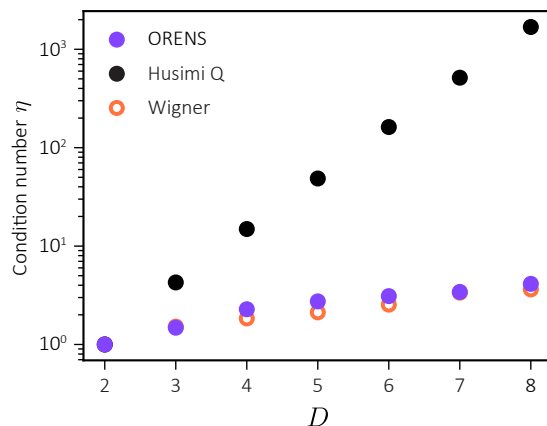


FIG. 11. Optimized condition number of ORENS, Wigner, and Husimi Q against truncation dimension of ρ .

3. Bayesian inference

Accurately inferring the quantum state of a system from measurement outcomes is a crucial task in quantum state reconstruction. In this section, we will motivate the use of Bayesian inference to process measurement outcomes and build the optimal estimator for ρ . For a deeper analysis, please refer to [37], and for details on the specific methodology used in our work, please refer to [24].

The most notable limitation of linear inversion is that the estimated ρ_{LS} frequently has negative eigenvalues, indicating that it cannot represent a physical state. Maximum likelihood estimation (MLE) was adopted as a

convenient way to impose physicality on ρ_{LS} , and has been the dominant approach to quantum state reconstruction in recent years. Intuitively, it returns a single non-negative state ρ_{MLE} that fits the observed data \mathcal{D} as precisely as possible by maximizing the likelihood function as

$$\rho_{MLE} = \arg \max_{\rho} L_{\mathcal{D}}(\rho) \quad (D5)$$

where $L_{\mathcal{D}}(\rho) \propto p(\mathcal{D}|\rho)$. It does not quantify the level of uncertainty of the result, and most critically, ρ_{MLE} often has zero eigenvalues. Consequently, it predicts exactly zero probability for every measurement outcome $|\psi\rangle\langle\psi|$ such that $\langle\psi|\rho|\psi\rangle = 0$. This implication of absolute certainty that a certain outcome will not be observed cannot reasonably be justified by a finite amount of data. The underlying flaw is that maximizing the likelihood is frequentistic by nature; it interprets the observed relative frequencies of the measurement outcomes as probabilities, and then seeks to fit the probabilities as precisely as possible. However, the goal of state estimation extends beyond explaining the data to predicting future evolutions and states. Thus, estimation should involve the knowledge of the system being estimated, especially its uncertainty.

In our work, we employed a Bayesian inference technique stemming from a different perspective on statistics that 1) considers many of the possible ρ , 2) accounts for experimental uncertainty explicitly through Bayes' rule, and 3) guarantees the most accurate estimate of the true ρ that can be made from the data [37, 50, 51]. Parameterizing $\rho(\mathbf{x})$ by some vector \mathbf{x} , such that any value of \mathbf{x} within its support returns a physical ρ , Bayes' theorem states that posterior probability distribution of \mathbf{x} follows as

$$\pi(\mathbf{x}) = \frac{1}{Z} L_D(\mathbf{x}) \pi_0(\mathbf{x}) \quad (D6)$$

where $L_D(\mathbf{x})$ is the same likelihood as in MLE, $\pi_0(\mathbf{x})$ is the prior distribution that encapsulates any knowledge or beliefs about ρ before the experiment, and Z a normalizing constant. This posterior distribution gives us access to the expectation value of any function ϕ of ρ via

$$\langle\phi(\rho)\rangle = \int d\mathbf{x} \pi(\mathbf{x}) \phi(\rho(\mathbf{x})) \quad (D7)$$

Evaluating integrals of this form is numerically challenging due to the high dimensionality and complicated features. We overcome this challenge by employing the efficient Bayesian inference strategy [24] that is computationally practical and straightforward to implement through a combination of well-chosen parameterization of ρ , likelihood, and Markov Chain Monte Carlo (MCMC) sampling algorithm. Intuitively, the algorithm draws random samples of possible ρ from a distribution across all physical states. These states are weighted by a pseudo-likelihood function that scales inversely with the distance

between the sample and ρ_{LS} . These samples allow us to estimate any function of ρ via

$$\langle\phi(\rho)\rangle \approx \frac{1}{R} \sum_{r=1}^R \phi(\rho_r) \quad (D8)$$

where R is the total number of MCMC samples. In detail, we chose the following parameters for Bayesian inference: $\alpha = 1$ for a uniform prior on all possible physical density matrices; $\sigma = 1/N$, $N = 1000(D^2 - 1)$ as the variance for the pseudo-likelihood function around ρ_{LS} ; 2^{10} MCMC samples with thinning parameter 2^7 to reduce serial correlation in the chain.

All simulated and experimental fidelities in this work were calculated with the ρ_{BME} ,

$$\rho_{BME} = \frac{1}{R} \sum_{r=1}^R \rho_r \quad (D9)$$

which stands as the most accurate estimator of the true ρ . Error bars represent the standard deviation across ρ_{BME} fidelities of all the set of reconstructed states (either Fock states or cat states). We demonstrate how the performance of BME surpasses that of MLE, as expected, in Table III and Table IV for ORENS reconstruction across dimensions and decoherence regimes, respectively.

D	\bar{F}_{BME}	\bar{F}_{MLE}	$\Delta = \bar{F}_{BME} - \bar{F}_{MLE}$
2	0.992	0.987	0.005
3	0.988	0.979	0.009
4	0.973	0.958	0.015
5	0.950	0.933	0.017
6	0.939	0.918	0.021

TABLE III. For each dimension, mean ORENS reconstruction fidelity using BME and MLE across all the Fock superposition states is recorded.

$T_{\phi}(\mu s)$	\bar{F}_{BME}	\bar{F}_{MLE}	$\Delta = \bar{F}_{BME} - \bar{F}_{MLE}$
22.4	0.947	0.932	0.015
10.4	0.946	0.927	0.018
3.48	0.944	0.931	0.013
1.02	0.875	0.856	0.019
0.535	0.867	0.851	0.016

TABLE IV. For engineered qubit T_2 , mean ORENS reconstruction fidelity using BME and MLE across all four cat states is recorded.

APPENDIX E: Estimation and simulation code

The code used to simulate ORENS with real hardware parameters and to process measurement outcomes and estimate ρ will be available on GitHub soon.

-
- [1] A. Copetudo, C. Y. Fontaine, F. Valadares, and Y. Y. Gao, Shaping photons: Quantum information processing with bosonic cQED, *Applied Physics Letters* **124**, 080502 (2024).
- [2] C. Weedbrook, S. Pirandola, R. García-Patrón, N. J. Cerf, T. C. Ralph, J. H. Shapiro, and S. Lloyd, Gaussian quantum information, *Reviews of Modern Physics* **84**, 621 (2012), publisher: American Physical Society.
- [3] X. Pan, P. Song, and Y. Y. Gao, Continuous-Variable Quantum Computation in Circuit QED, *Chinese Physics Letters* **40**, 110303 (2023), publisher: Chinese Physical Society and IOP Publishing Ltd.
- [4] A. Joshi, K. Noh, and Y. Y. Gao, Quantum information processing with bosonic qubits in circuit QED, *Quantum Science and Technology* **6**, 033001 (2021), publisher: IOP Publishing.
- [5] P. Campagne-Ibarcq, A. Eickbusch, S. Touzard, E. Zalys-Geller, N. E. Frattini, V. V. Sivak, P. Reinhold, S. Puri, S. Shankar, R. J. Schoelkopf, L. Frunzio, M. Mirrahimi, and M. H. Devoret, Quantum error correction of a qubit encoded in grid states of an oscillator, *Nature* **584**, 368 (2020), publisher: Nature Publishing Group.
- [6] Y. Y. Gao, B. J. Lester, K. S. Chou, L. Frunzio, M. H. Devoret, L. Jiang, S. M. Girvin, and R. J. Schoelkopf, Entanglement of bosonic modes through an engineered exchange interaction, *Nature* **566**, 509 (2019), publisher: Nature Publishing Group.
- [7] W. Wang, Y. Wu, Y. Ma, W. Cai, L. Hu, X. Mu, Y. Xu, Z.-J. Chen, H. Wang, Y. P. Song, H. Yuan, C.-L. Zou, L.-M. Duan, and L. Sun, Heisenberg-limited single-mode quantum metrology in a superconducting circuit, *Nature Communications* **10**, 4382 (2019), publisher: Nature Publishing Group.
- [8] K. Liu, Y. Xu, W. Wang, S.-B. Zheng, T. Roy, S. Kundu, M. Chand, A. Ranadive, R. Vijay, Y. Song, L. Duan, and L. Sun, A twofold quantum delayed-choice experiment in a superconducting circuit, *Science Advances* **3**, e1603159 (2017), publisher: American Association for the Advancement of Science.
- [9] O. Landon-Cardinal, L. C. Govia, and A. A. Clerk, Quantitative Tomography for Continuous Variable Quantum Systems, *Physical Review Letters* **120**, 090501 (2018), publisher: American Physical Society.
- [10] K. He, M. Yuan, Y. Wong, S. Chakram, A. Seif, L. Jiang, and D. I. Schuster, Efficient multimode Wigner tomography (2023), arXiv:2309.10145 [cond-mat, physics:quant-ph].
- [11] S. Chakram, K. He, A. V. Dixit, A. E. Oriani, R. K. Naik, N. Leung, H. Kwon, W.-L. Ma, L. Jiang, and D. I. Schuster, Multimode photon blockade, *Nature Physics* **18**, 879 (2022), number: 8 Publisher: Nature Publishing Group.
- [12] C. Shen, R. W. Heeres, P. Reinhold, L. Jiang, Y.-K. Liu, R. J. Schoelkopf, and L. Jiang, Optimized tomography of continuous variable systems using excitation counting, *Physical Review A* **94**, 052327 (2016).
- [13] C. Wang, Y. Y. Gao, P. Reinhold, R. W. Heeres, N. Ofek, K. Chou, C. Axline, M. Reagor, J. Blumoff, K. M. Sliwa, L. Frunzio, S. M. Girvin, L. Jiang, M. Mirrahimi, M. H. Devoret, and R. J. Schoelkopf, A Schrödinger cat living in two boxes, *Science* **352**, 1087 (2016), publisher: American Association for the Advancement of Science.
- [14] B. Calkins, P. L. Mennea, A. E. Lita, B. J. Metcalf, W. S. Kolthammer, A. Lamas-Linares, J. B. Spring, P. C. Humphreys, R. P. Mirin, J. C. Gates, P. G. R. Smith, I. A. Walmsley, T. Gerrits, and S. W. Nam, High quantum-efficiency photon-number-resolving detector for photonic on-chip information processing, *Optics Express* **21**, 22657 (2013), publisher: Optica Publishing Group.
- [15] M. Brune, F. Schmidt-Kaler, A. Maali, J. Dreyer, E. Hæggly, J. M. Raimond, and S. Haroche, Quantum Rabi Oscillation: A Direct Test of Field Quantization in a Cavity, *Physical Review Letters* **76**, 1800 (1996), publisher: American Physical Society.
- [16] C. Guerlin, J. Bernu, S. Deléglise, C. Sayrin, S. Gleyzes, S. Kuhr, M. Brune, J.-M. Raimond, and S. Haroche, Progressive field-state collapse and quantum non-demolition photon counting, *Nature* **448**, 889 (2007), number: 7156 Publisher: Nature Publishing Group.
- [17] D. I. Schuster, A. A. Houck, J. A. Schreier, A. Wallraff, J. M. Gambetta, A. Blais, L. Frunzio, J. Majer, B. Johnson, M. H. Devoret, S. M. Girvin, and R. J. Schoelkopf, Resolving photon number states in a superconducting circuit, *Nature* **445**, 515 (2007), publisher: Nature Publishing Group.
- [18] H. Wang, M. Hofheinz, M. Ansmann, R. C. Bialczak, E. Lucero, M. Neeley, A. D. O'Connell, D. Sank, M. Weides, J. Wenner, A. N. Cleland, and J. M. Martinis, Decoherence Dynamics of Complex Photon States in a Superconducting Circuit, *Physical Review Letters* **103**, 200404 (2009), publisher: American Physical Society.
- [19] D. Leibfried, D. M. Meekhof, B. E. King, C. Monroe, W. M. Itano, and D. J. Wineland, Experimental Determination of the Motional Quantum State of a Trapped Atom, *Physical Review Letters* **77**, 4281 (1996), publisher: American Physical Society.
- [20] S. An, J.-N. Zhang, M. Um, D. Lv, Y. Lu, J. Zhang, Z.-Q. Yin, H. T. Quan, and K. Kim, Experimental test of the quantum Jarzynski equality with a trapped-ion system, *Nature Physics* **11**, 193 (2015), number: 2 Publisher: Nature Publishing Group.
- [21] H.-Y. Lo, D. Kienzler, L. de Clercq, M. Marinelli, V. Negnevitsky, B. C. Keitch, and J. P. Home, Spin-motion entanglement and state diagnosis with squeezed oscillator wavepackets, *Nature* **521**, 336 (2015), number: 7552 Publisher: Nature Publishing Group.
- [22] L. G. Lutterbach and L. Davidovich, Method for Direct Measurement of the Wigner Function in Cavity QED and Ion Traps, *Physical Review Letters* **78**, 2547 (1997), publisher: American Physical Society.
- [23] P. Bertet, A. Auffèves, P. Maioli, S. Osnaghi, T. Meunier, M. Brune, J. M. Raimond, and S. Haroche, Direct Measurement of the Wigner Function of a One-Photon Fock State in a Cavity, *Physical Review Letters* **89**, 200402 (2002), publisher: American Physical Society.
- [24] J. M. Lukens, K. J. H. Law, A. Jasra, and P. Lougovski, A practical and efficient approach for Bayesian quantum state estimation, *New Journal of Physics* **22**, 063038 (2020).
- [25] R. Bhatia, *Matrix Analysis*, Graduate Texts in Mathematics, Vol. 169 (Springer, New York, NY, 1997).
- [26] G. Kirchmair, B. Vlastakis, Z. Leghtas, S. E. Nigg, H. Paik, E. Ginossar, M. Mirrahimi, L. Frunzio, S. M.

- Girvin, and R. J. Schoelkopf, Observation of quantum state collapse and revival due to the single-photon Kerr effect, *Nature* **495**, 205 (2013), number: 7440 Publisher: Nature Publishing Group.
- [27] T. Opatrný and D.-G. Welsch, Density-matrix reconstruction by unbalanced homodyning, *Physical Review A* **55**, 1462 (1997), publisher: American Physical Society.
- [28] J. S. Lundeen, A. Feito, H. Coldenstrodt-Ronge, K. L. Pregnell, C. Silberhorn, T. C. Ralph, J. Eisert, M. B. Plenio, and I. A. Walmsley, Tomography of quantum detectors, *Nature Physics* **5**, 27 (2009), number: 1 Publisher: Nature Publishing Group.
- [29] L. Zhang, H. B. Coldenstrodt-Ronge, A. Datta, G. Puentes, J. S. Lundeen, X.-M. Jin, B. J. Smith, M. B. Plenio, and I. A. Walmsley, Mapping coherence in measurement via full quantum tomography of a hybrid optical detector, *Nature Photonics* **6**, 364 (2012), number: 6 Publisher: Nature Publishing Group.
- [30] T. B. Smith, Generalized Q-functions, *Journal of Physics A: Mathematical and General* **39**, 13747 (2006).
- [31] R. W. Heeres, P. Reinhold, N. Ofek, L. Frunzio, L. Jiang, M. H. Devoret, and R. J. Schoelkopf, Implementing a universal gate set on a logical qubit encoded in an oscillator, *Nature Communications* **8**, 94 (2017), number: 1 Publisher: Nature Publishing Group.
- [32] M. Kjaergaard, M. E. Schwartz, J. Braumüller, P. Krantz, J. I.-J. Wang, S. Gustavsson, and W. D. Oliver, Superconducting Qubits: Current State of Play, *Annual Review of Condensed Matter Physics* **11**, 369 (2020), eprint: <https://doi.org/10.1146/annurev-comatphys-031119-050605>.
- [33] O. Gargiulo, S. Oleschko, J. Prat-Camps, M. Zanner, and G. Kirchmair, Fast flux control of 3D transmon qubits using a magnetic hose, *Applied Physics Letters* **118**, 012601 (2021).
- [34] M. Hutchings, J. Hertzberg, Y. Liu, N. Bronn, G. Keefe, M. Brink, J. M. Chow, and B. Plourde, Tunable Superconducting Qubits with Flux-Independent Coherence, *Physical Review Applied* **8**, 044003 (2017), publisher: American Physical Society.
- [35] A. P. Sears, A. Petrenko, G. Catelani, L. Sun, H. Paik, G. Kirchmair, L. Frunzio, L. I. Glazman, S. M. Girvin, and R. J. Schoelkopf, Photon shot noise dephasing in the strong-dispersive limit of circuit QED, *Physical Review B* **86**, 180504 (2012), publisher: American Physical Society.
- [36] R. Blume-Kohout and P. Hayden, Accurate quantum state estimation via "Keeping the experimentalist honest" (2006), arXiv:quant-ph/0603116.
- [37] R. Blume-Kohout, Optimal, reliable estimation of quantum states, *New Journal of Physics* **12**, 043034 (2010).
- [38] J. A. Smolin, J. M. Gambetta, and G. Smith, Efficient Method for Computing the Maximum-Likelihood Quantum State from Measurements with Additive Gaussian Noise, *Physical Review Letters* **108**, 070502 (2012), publisher: American Physical Society.
- [39] J. Joo, W. J. Munro, and T. P. Spiller, Quantum Metrology with Entangled Coherent States, *Physical Review Letters* **107**, 083601 (2011), publisher: American Physical Society.
- [40] T. C. Ralph, A. Gilchrist, G. J. Milburn, W. J. Munro, and S. Glancy, Quantum computation with optical coherent states, *Physical Review A* **68**, 042319 (2003), publisher: American Physical Society.
- [41] C. Chamberland, K. Noh, P. Arrangoiz-Arriola, E. T. Campbell, C. T. Hann, J. Iverson, H. Putterman, T. C. Bohdanowicz, S. T. Flammia, A. Keller, G. Refael, J. Preskill, L. Jiang, A. H. Safavi-Naeini, O. Painter, and F. G. Brandão, Building a Fault-Tolerant Quantum Computer Using Concatenated Cat Codes, *PRX Quantum* **3**, 010329 (2022), publisher: American Physical Society.
- [42] N. Ofek, A. Petrenko, R. Heeres, P. Reinhold, Z. Leghtas, B. Vlastakis, Y. Liu, L. Frunzio, S. M. Girvin, L. Jiang, M. Mirrahimi, M. H. Devoret, and R. J. Schoelkopf, Extending the lifetime of a quantum bit with error correction in superconducting circuits, *Nature* **536**, 441 (2016), publisher: Nature Publishing Group.
- [43] S. Puri, L. St-Jean, J. A. Gross, A. Grimm, N. E. Frattini, P. S. Iyer, A. Krishna, S. Touzard, L. Jiang, A. Blais, S. T. Flammia, and S. M. Girvin, Bias-preserving gates with stabilized cat qubits, *Science Advances* **6**, eaay5901 (2020), publisher: American Association for the Advancement of Science.
- [44] X. Pan, Protecting the Quantum Interference of Cat States by Phase-Space Compression, *Physical Review X* **13**, 10.1103/PhysRevX.13.021004 (2023).
- [45] A. Blais, R.-S. Huang, A. Wallraff, S. M. Girvin, and R. J. Schoelkopf, Cavity quantum electrodynamics for superconducting electrical circuits: An architecture for quantum computation, *Physical Review A* **69**, 062320 (2004), publisher: American Physical Society.
- [46] S. M. Girvin, Circuit QED: superconducting qubits coupled to microwave photons, in *Quantum Machines: Measurement and Control of Engineered Quantum Systems*, edited by M. Devoret, B. Huard, R. Schoelkopf, and L. F. Cugliandolo (Oxford University Press Oxford, 2014) 1st ed., pp. 113–256.
- [47] Z. K. Mineev, Z. Leghtas, S. O. Mundhada, L. Christakis, I. M. Pop, and M. H. Devoret, Energy-participation quantization of Josephson circuits, *npj Quantum Information* **7**, 1 (2021), number: 1 Publisher: Nature Publishing Group.
- [48] Y. Sunada, S. Kono, J. Ilves, S. Tamate, T. Sugiyama, Y. Tabuchi, and Y. Nakamura, Fast Readout and Reset of a Superconducting Qubit Coupled to a Resonator with an Intrinsic Purcell Filter, *Physical Review Applied* **17**, 044016 (2022).
- [49] D. McClure, H. Paik, L. Bishop, M. Steffen, J. M. Chow, and J. M. Gambetta, Rapid Driven Reset of a Qubit Readout Resonator, *Physical Review Applied* **5**, 011001 (2016), publisher: American Physical Society.
- [50] B. P. Williams and P. Lougovski, Quantum state estimation when qubits are lost: a no-data-left-behind approach*, *New Journal of Physics* **19**, 043003 (2017), publisher: IOP Publishing.
- [51] C. Granade, J. Combes, and D. G. Cory, Practical Bayesian tomography, *New Journal of Physics* **18**, 033024 (2016), publisher: IOP Publishing.